ACS BIO & MED CHEM Au
AN OPEN ACCESS JOURNAL OF THE AMERICAN CHEMICAL SOCIETY

Engineering Cell-Specific Protein Delivery Vehicles for Erythroid Lineage Cells

Published as part of ACS Bio & Med Chem Au special issue "2024 Rising Stars in Biological, Medicinal, and Pharmaceutical Chemistry".

Mekedlawit T. Setegne, Aidan T. Cabral, Anushri Tiwari, Fangfang Shen, Hawa Racine Thiam, and Laura M. K. Dassama*

Cite This: *ACS Bio Med Chem Au* 2025, 5, 268−282

Read Online

ACCESS | Metrics & More | Article Recommendations | SI Supporting Information

ABSTRACT: Biologics such as proteins, peptides, and oligonucleotides are powerful ligands to modulate challenging drug targets that lack readily accessible and "ligandable" pockets. However, the limited membrane permeance of biologics severely restricts their intracellular applications. Moreover, different cell types may exhibit varying levels of impermeability, and some delivery vehicles might be more sensitive to this variance. Erythroid lineage cells are especially challenging to deliver cargo to because of their unique cytoskeleton and the absence of endocytosis in mature erythrocytes. We recently employed a cell permeant miniature protein to deliver bioPROTACs to human umbilical cord blood derived erythroid progenitor cells (HUDEP-2) and primary hematopoietic stem ($CD34^+$) cells (Shen et al., *ACS Cent. Sci.* **2022**, *8*, 1695−1703). While successful, the low efficiency of delivery and lack of cell-type specificity limit use of bioPROTACs *in vivo*. In this work, we thoroughly evaluated the performance of various recently reported cell penetrating peptides (CPPs), CPP additives, bacterial toxins, and contractile injection systems for their ability to deliver cargo to erythroid precursor cells. We also explored how targeting receptors enriched on the erythroid cell surface might improve the efficiencies and specificities of these delivery vehicles. Our results reveal that certain vehicles exhibit improved efficiencies when directed to cell surface receptors while others do not benefit from this targeting strategy. Together, these findings advance our understanding of protein delivery to challenging cell types and illustrate some of the intricacies of cell-surface receptor targeting.

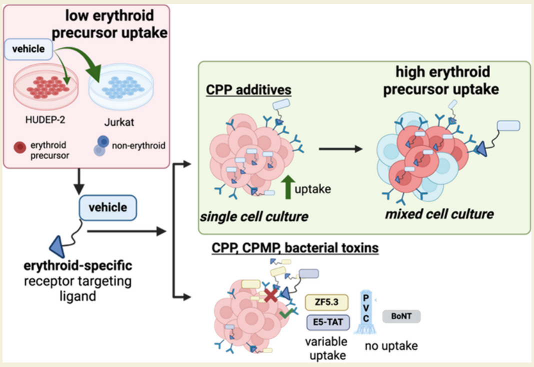

KEYWORDS: *protein delivery, intracellular delivery, erythroid lineage cells, permeant peptides, quantitative cell imaging*

INTRODUCTION

85% of the disease-causing human proteome has yet to be targeted with traditional small molecules and is considered "undruggable".[1] This perceived "undruggability" is because these proteins, which comprise transcription factors, non-enzymatic proteins, and scaffolding proteins, frequently lack binding pockets for traditional inhibitors.[1−3] Instead, many exert their function through interactions at large, shallow protein−protein interfaces or highly disordered regions. The development of biologics such as protein, peptide, and oligonucleotide binders provides an avenue to modulate the functions of challenging disease-relevant targets.[4−6] While biologics are highly specific, well-tolerated, and can target the "undruggable proteome", their low membrane permeance limits their effectiveness against intracellular protein targets. As such, the intracellular delivery of functional biologics continues to be a major bottleneck for both basic science discoveries and the translation of promising biologics-based drug candidates.[7]

Genetic methods are commonly used to study novel protein-based biologics for intracellular targets. These involve intracellular gene delivery followed by the expression of biologics and downstream functional and mechanistic studies.[8,9] Yet, gene delivery via viral-based transfection methods takes longer to process the active biomolecule, may cause permanent genome change, and result in immunogenicity and cytotoxicity.[10,11] Alternatively, the delivery of proteins allows for direct investigation of protein function without permanent changes to the cell state. Moreover, it elicits a faster response than gene delivery by bypassing the need for subsequent protein production, enabling immediate target engagement and

Received: September 23, 2024
Revised: February 11, 2025
Accepted: February 11, 2025
Published: February 27, 2025

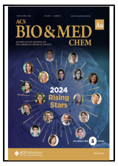

https://doi.org/10.1021/acsbiomedchemau.4c00098

modulation with precise control over the treatment dosage. Additionally, protein delivery allows for easy exogenous modification of biologic cargos.[10,12]

Intracellular protein delivery has been achieved with delivery vehicle (DV) types that include nanoparticles,[13−15] viruses,[16,17] and protein-based translocation agents.[18−22] While these all have unique advantages, the encapsulation of protein molecules into nanoparticles and viruses is not trivial and often has size and charge restrictions.[10] On the other hand, the use of protein-based vehicles and engineering efforts to improve permeability of cells or permeance of cargos provide simplicity and versatility for protein delivery. Furthermore, engineered protein DVs can readily be synthesized or genetically encoded to deliver a range of cargo.[18]

Most protein DVs provide a means to deliver protein cargos to intracellular targets through direct penetration of the plasma membrane or through endocytosis and subsequent endosomal escape.[23−26] Their mechanisms encompass charge-induced transport,[27,28] permeabilization of membrane through disulfide reactivity,[29] receptor-mediated endocytosis,[30] and direct injection through force application.[31] However, their efficiencies in delivering cargo can vary greatly across cell types,[32] most likely due to differences in membrane lipid composition[33,34] and proteins that associate with those lipids;[35,36] this limits their use in complex *in vitro* and *in vivo* models. For example, there are few reports of the use of protein DVs to deliver cargo into erythroid cell lines. Erythroid and precursor cells contain spectrin tetramers in their cytoskeleton, which further complicates the delivery of large molecules to their cytosol.[37,38] Yet, erythroid-specific diseases such as sickle cell disease could benefit from the delivery of functional protein cargo to diseased cells.[39]

A recent report from our group demonstrated the use of a cell permeant protein-based degrader, or bioPROTAC, specific for the transcriptional repressor BCL11A. BCL11A controls the switch from fetal to adult-type hemoglobin in erythroid precursor cells and is the target of recent sickle cell disease therapies. To achieve cell permeance with the bioPROTAC, the cell permeant miniature protein (CPMP) ZF5.3 was fused to a nanobody-based degrader. Treatment of HUDEP-2 and CD34$^+$ cells with the bioPROTAC resulted in depletion of up to 70% of BCL11A.[40] While this platform provided a modular method for developing cell permeant bioPROTACs, key limitations, such as the delivery efficiency and cell type specificity, remain. Due to the low total uptake of the bioPROTAC, we herein compared efficiencies of established delivery vehicles for delivering protein cargo to developing erythrocytes by measuring total uptake; it should be noted that this study does not distinguish cytosolic delivery from delivery to other cellular compartments. We additionally investigated whether the uptake efficiency and specificity of the vehicles could be improved with the addition of a cell surface targeting moiety. In this report, we used both confocal microscopy and flow cytometry to compare and quantify the total uptake between vehicles. It is important to note that while our work focuses on total cellular uptake and only uses colocalization in confocal microscopy images to qualitatively distinguish cellular compartments (such as endosomes and cytosol), other techniques such as fluorescence correlation spectroscopy and split luciferase endosomal escape quantification (SLEEQ) can better estimate the amount of protein in the cytosol. We additionally investigated whether the uptake efficiency and specificity of the vehicles could be improved with the addition of a cell surface targeting moiety. By employing the nanobody IH4, which binds to the erythroid lineage-specific receptor glycophorin A (GYPA)[41−43] with nanomolar range equilibrium dissociation constant (K_d),[44] we observed that certain DVs had significant improvement in uptake efficiencies while others had unchanged or decreased efficiencies. We also investigated the ability of IH4 to provide specificity for cargo delivery to GYPA expressing cells in mixed cell populations and observed a striking accumulation of cargo in GYPA expressing cells. Together, our findings revealed that the DVs exhibit different responses to the presence of targeting moieties and highlight that in addition to considerations regarding the cargo, cell type and targeting moieties should be considered when selecting DVs for intracellular protein delivery.

■ MATERIALS AND METHODS

Plasmid Construction

All gene blocks (Table S1) were obtained from Azenta Life Sciences. The DNA encoding mNeonGreen with a C-terminal hexa-histidine (6 × His) tag was obtained from the Phillip Kyriakakis Group at Stanford University and was modified from Addgene #182413. Primers (Table S2) were obtained from Integrated DNA Technologies. KOD hot start polymerase (Novagen #71316) was used for PCR reactions, while NEBuilder HiFi DNA Assembly (New England Biolabs, #E2621) was used for plasmid fusions. NdeI (New England Biolabs #R0111) and XhoI (New England Biolabs #R0146) were used to digest plasmids. Primary sequences of all constructs can be found in Table S2 and primers in Table S3.

IH4. The sequence for the IH4 nanobody was codon-optimized for expression in *Escherichia coli* and cloned into a linearized pET-20b vector using the NdeI and XhoI sites.

mNG-IH4 and IH4-mNG. The sequence of mNeonGreen was amplified from pRSFDuet-mNeonGreen using primers and cloned into a linearized pET-20b-IH4 vector using HiFi.

ZF5.3-mNG. The plasmid encoding ZF5.3 was gifted from the Alanna Schepartz Group at the University of California, Berkeley. The sequence of ZF5.3 was codon-optimized for expression in *E. coli* and cloned into a linearized pet32a vector with a C-terminal 6 × His tag; the sequence of mNeonGreen was amplified from pRSFDuet-mNeonGreen using primers reported in Table S3.

ZF5.3-mNG-IH4. The sequence of IH4 was amplified from pet20b-IH4 and cloned into a linearized pet32a-ZF5.3-mNeonGreen vector with a C-terminal 6× His tag.

E5TAT-mNG. The sequence of E5TAT was codon-optimized for expression in *E. coli* and cloned into a linearized pet32a-mNeonGreen vector with a C-terminal 6× His tag.

E5TAT-mNG-IH4. The sequence of IH4 was amplified from pet20b-IH4 and cloned into a linearized pet32a-E5TAT-mNeonGreen vector with a C-terminal 6× His tag.

mNG-BoNT-IH4 and mNG-BoNT. The sequence of inactivated BoNT was codon-optimized for expression in *E. coli* and cloned into the pet20b-mNG-IH4 or pet20b-mNG vector. Following this, mNG-BoNT-IH4 and mNG-BoNT were amplified from pet20b-mNG-BoNT-IH4 and cloned into pGEX-KG backbone vector (gifted from the Alice Ting Group at Stanford University) with a N-terminal GST tag and TEV cleavage site.

pAWP78-PVCpnf_pvc13-Ad5 Knob and PVC_pvc13-IH4. The pAWP78-PVCpnf_pvc13-Ad5Knob (Addgene #198289) and pBR322-PVCpnf17−22 (Addgene #198272) were ordered from Addgene. The sequence for the 6×GSSG-IH4−2×GSSG insert was codon-optimized for expression in *E. coli* and cloned into linearized pAWP78-PVCpnf_pvc13 using the primers reported in Table S3.

Transformation

2 μL of each plasmid (concentration ≥20 ng/μL) was transformed into BL21 (DE3) cells, except for *Photorhabdus* virulence cassette (PVC) constructs for which 50−100 ng were electroporated into EPI300 electrocompetent cells (Lucigen #EC300110). BL21 (DE3) cells were incubated on ice for 15 min, and cells were heat shocked at 42 °C for 45 s and placed on ice for 2 min. The cells were recovered with the addition

of 900 μL of Luria Broth (LB) media for 30 min at 37 °C while shaking at 200 rpm. Cells were centrifuged for 3 min at 2500 × *g* and resuspended in 100 μL of media before plated to LB-agar plates supplemented with either ampicillin (100 μg/mL), kanamycin (100 μg/mL), or Kan/Amp plates (100 μg/mL each) and incubated at 37 °C overnight.

Protein Production

General His-Tag Protein Purification. Vectors encoding the genes of 6× His tagged proteins were used to transform *E. coli* BL21 (DE3) competent cells. Individual colonies were selected and used to inoculate 50 mL of LB medium supplemented with Amp or Kan (100 μg/mL). The primary culture was grown overnight and then used to inoculate 6 L of LB media supplemented with Amp or Kan and allowed to grow at 37 °C while being shaken at 200 rpm. When the $O.D._{600\ nm}$ reached 0.6−0.8, the temperature was changed to 18 °C and 0.5 mM (for mNG, IH4-mNG, mNG-IH4) or 0.75 mM (for ZF5.3-mNG, ZF5.3-mNG-IH4) of isopropyl β-D-1-thiogalactopyranoside (IPTG) was added. The cells were cultured overnight and harvested by centrifugation at 6000 × *g* for 30 min at 4 °C. After that, cells were resuspended in buffer containing 50 mM Tris-HCl at pH 8.0, 500 mM NaCl, and 1 mM PMSF and lysed via microfluidization. For ZF5.3 and E5TAT constructs, buffers were the same but with the addition of 5 mM 2-mercaptoethanol and 100 μM $ZnSO_4$ to stabilize ZF5.3 constructs. The lysate was then clarified by centrifuging at 15,000 × *g* for 30 min at 4 °C. The protein was purified via Ni-NTA affinity chromatography (HiTrap IMAC FF, Cytiva no. 17092104) by washing with lysis buffer supplemented with 10 mM imidazole to remove weakly bound proteins and eluted with lysis buffer containing 300 mM imidazole. The eluate was concentrated, and buffer was exchanged to 50 mM Tris-HCl pH 8.0, 150 mM NaCl using 10 kDa MWCO spin concentrators (Millipore #UFC9010) and applied to a size-exclusion column (HiLoad 16/600 Superdex 200 pg, Cytiva #28989335) to remove additional contaminants; purity was assessed through gel electrophoresis. Pure proteins were concentrated, flash frozen in liquid nitrogen, and stored at −80 °C for further use. For downstream cell delivery assays, all proteins were exchanged into dPBS buffer (Gibco #14190094) using PD-10 columns (Cytivia #17085101), and concentrations were determined using the Pierce BCA Protein Assay Kit (Thermo Scientific, #PI23235) with a Nanodrop OneC (Thermo Scientific) according to the manufacturer's instruction.

mNG-BoNT, mNG-BoNT-IH4. Plasmids encoding GST-mNG-BoNT and GST-mNG-BoNT-IH4 constructs were transformed into *E. coli* BL21 (DE3) competent cells. Single colonies were used to inoculate 50 mL of LB supplemented with 100 mg/L ampicillin and grown overnight at 37 °C and 200 rpm. The overnight seed culture was diluted 1:100 into LB-Amp and was incubated at 37 °C, 200 rpm, until the $O.D._{600\ nm}$ was 0.4−0.6. Protein production was then induced by adding 0.2 mM IPTG and the cells were grown overnight at 25 °C and 200 rpm. After that, the cells were harvested by centrifugation at 6000 × *g* for 30 min at 4 °C and resuspended in buffer containing 50 mM Tris-HCl, pH 8.0, 500 mM NaCl, 5 mM EDTA, 1 mM DTT, and 1 mM PMSF. Cells were lysed via microfluidization. The lysate was clarified by centrifuging at 15,000 × *g* for 30 min at 4 °C, and the cleared lysate was added to Pierce Glutathione Agarose resin (GST, Pierce Cat #16100), following manufacturer's protocols. Briefly the clarified lysate was incubated with GST resin for at least 1 h at 4 °C. After this, the resin was washed with lysis buffer to remove weakly bound proteins. The bound protein was eluted using lysis buffer supplemented with freshly made 1 mM DTT and 10 mM reduced glutathione. Eluted proteins were exchanged into dPBS buffer using 100 kDa MWCO spin concentrators (Millipore #UFC9100). Finally, mNG-BoNT-IH4 was incubated with 10U/mg of Thrombin (Sigma-Aldrich catalog no. T6634) overnight at 4 °C to cleave the GST tag. After cleavage, residual thrombin and the cleaved GST tag were removed using 50 kDa MWCO spin concentrators (Millipore #UFC9050).

pAWP78-PVCpnf with pvc13-Ad5Knob or PVC_pvc13-IH4. For each PVC condition, one variant each of pPVC (pvc13-Ad5Knob or PVC_pvc13-IH4) and payload (pAWP78-PVCpnf) were electroporated into EPI300 cells, and PVC particles were purified using a modified version of a method reported previously.[31] Briefly, colonies were inoculated into 2 mL of Terrific Broth (US Biological T2810) and shaken at 37 °C for 16 h before being inoculated (at 1:1,000) into 500 mL of TB and shaken at 30 °C for an additional 24 h. Cultures were then centrifuged for 30 min at 4,000 × *g* and resuspended in 28 mL of lysis buffer (25 mM Tris-HCl pH 7.5, 140 mM NaCl, 3 mM KCl, 5 mM $MgCl_2$, 200 μg/mL lysozyme, 50 μg/mL DNase I, 0.5% Triton X-100, and protease inhibitor cocktail (Bimake, #B14002)); the cells were subsequently shaken at 37 °C for 90−120 min to promote lysis. Lysates were pelleted at 4,000 × *g* for 30 min at 4 °C to remove bulk cell lysate. The supernatant was then extracted and centrifuged in an ultracentrifuge at 120,000 × *g* for 1.5 h at 4 °C to pellet PVC protein complexes. Pellets were resuspended in 1 mL of PBS buffer (Life Technologies 10010049) and centrifuged at 16,000 × *g* for 15 min at 4 °C to remove residual solids. Supernatants were diluted with 28 mL of cold PBS buffer, ultracentrifuged again (120,000 × *g* for 2 h followed by a clarification spin at 16,000 × *g* for 15 min) twice. Final pellets were resuspended in 50−100 μL of PBS buffer, and the PVC yield was quantified by the absorbance at 280 nm on a NanoDrop instrument.

General Cell Culture

HUDEP-2 cells (Riken RCB4557) were obtained from the Riken BioResource Research Center (Japan). In brief, cells were maintained in expansion medium, which contains StemSpan serum-free expansion medium (SFEM, Stemcell Technologies), 2% Penicillin-Streptomycin solution (10,000 U/mL stock), 50 ng/mL recombinant human stem cell factor (SCF, Stemcell Technologies), 3 IU/mL Epoetin alfa (Epogen, Amgen), 0.4 μg/mL dexamethasone, and 1 μg/mL doxycycline. Jurkat were maintained in RPMI 1640 (Gibco #11875093) with 10% heat-inactivated fetal bovine serum (FBS, #16140071) and 100 U/mL penicillin/streptomycin (Gibco #15140122). Human HEK293T cells (female) were purchased from ATCC. The cells were cultured in DMEM, high glucose (Thermo Fisher Scientific, 11965) with 10% FCS and 2 mM L-Glutamine. All cells were cultured at 37 °C in the presence of 5% CO_2. For uptake assays, unenriched IMDM media (Cytiva no. SH30228.02) without FBS.

TNB-R10 Synthesis

Cys-R10 peptide with a 2 × PEG linker was synthesized by Biomatik. Cys-R10 was reacted with 10 equiv of Ellman's reagent (5,5′-dithiobis(2-nitrobenzoic acid), TNB), and the resulting peptide was purified by reverse-phase HPLC, as previously reported.[45] Preparative HPLC of peptides was performed on the following gradient: A = H_2O + 0.1% TFA, B = MeCN + 0.1% TFA 5% B 0−10 min, 5−50% B 10−30 min, 50−99% 30−40 min via high-performance liquid chromatography (HPLC) on a C18 semiprep column.

Protein Modification and Uptake

Proteins (100 μM) were modified with varying molar equivalents of Traut's reagent (2-iminothiolane) for 1 h at room temperature. Excess reagent was immediately removed using a desalting column (Zeba, no. 89877), and the protein was exchanged into dPBS. All other experiments used 5 equiv of Traut's reagent as described above; all samples were freshly modified and immediately used for delivery assays.

Protein and TNB-R10 Conjugation

Proteins were diluted to 5 or 25 μM in dPBS, treated with 1 or 3 equiv of TNB-R10, and incubated for 30 min−1 h at room temperature. The modified protein-peptide solutions were directly diluted to 1 or 5 μM with cell media, SFEM, IMDM, or RPMI 1640 and used in cell experiments.

Quantification of TNB-R10 Molecules Conjugated Per Protein Molecule

100 μM mNG or IH4-mNG was reacted with either 0 or 5 equiv of 2-iminothiolane as described above to make either mNG (0×) and IH4-mNG (0×) or mNG (5×) and IH4-mNG (5×). 100 μM mNG (0×), IH4-mNG (0×), mNG (5×), and IH4-mNG (5×) were reacted with either 0, 1, or 3 equiv of TNB-R10 for 1 h at room temperature. Excess TNB-R10 was removed using a desalting column (Zeba, #89877), and proteins were diluted to make 10 μM stock. 500 μM Ellman's reagent

(5,5′-dithiobis(2-nitrobenzoic acid, TNB) stock solution was prepared in dPBS. 10 μM protein stock solution was mixed with 1:1 with 500 μM of Ellman's reagent (5,5′-dithiobis(2-nitrobenzoic acid, TNB) stock solution for a final concentration of 5 μM protein and 250 μM TNB. The mixture was incubated for 30 min at room temperature before the absorbance at 412 nm was recorded on a plate reader (Tecan Spark). The number of reactive cysteines per protein can be calculated by fitting the absorption values into the Beer−Lambert equation: $(A_{sample} - A_{blank}) = \varepsilon cl$, where A = Absorbance, ε = molar extinction coefficient of TNB (14,150 M^{-1} cm^{-1} at A_{412} nm), c = concentration of TNB (which is equal to the concentration of free surface accessible cysteines of the protein), and l is the absorption path length. The number of accessible cysteines per protein was calculated by dividing the number of moles of cysteines by the number of moles of protein.[46] The amount of TNB-R10 decorated is estimated by comparing the number of accessible cysteines before and after incubation of TNB-R10, with the assumption that a decrease in accessible cysteines implies formation of covalent bonds with free TNB-R10.

General Cellular Uptake Assay and Viability Studies

5×10^5 cells/mL of Jurkat, HUDEP-2, or 1:1 Jurkat:HUDEP-2 cells were washed with dPBS twice and seeded into 96-well plates. Single cells were either incubated with protein for 1 h in unenriched media (IMDM) and then recovered without protein in full expansion medium (RPMI, SFEM) at 37 °C for an additional 1 h (Figures 2, 3, and 5) or incubated with protein for 2 h in full expansion medium 1:1 RPMI:SFEM at 37 °C (Figures 4, 6). Mixed cells were incubated with protein for 2 h in full expansion medium 1:1 RPMI:SFEM at 37 °C (Figure 7). Cells were collected by centrifugation (300 × *g* for 5 min), washed 3× with 500 μL of PBS buffer, and prepared for downstream analysis. Control samples were cells treated with unmodified mNG with no DV appended. The impact on viability was assessed upon delivery of the highest dosage used in the delivery assays (8 μM for samples without IH4 and 5 μM for samples containing IH4). Briefly, cells were incubated at 500,000/mL with constructs for 1 h in unenriched media at 37 °C. Cells were then revived for 24 h, after which their viability was assessed using CellTiter-Glo 2.0 assay kit (Promega, #G9241).

Live Cell Spinning Disc Confocal Imaging and Quantification of Cellular Uptake

Cells were treated as described above (see section on *Cellular uptake assay and viability studies*) with a final concentration of either 1, 5, or 8 μM protein in the media and were subsequently washed with dPBS 3 times. The cells were first incubated with 1 μg/mL of DAPI in dPBS for 10 min at 37 °C, 5% CO_2 to label dead cells. Cells were spun down and resuspended in staining solution with CellMask (1 μM for 1 h, Thermo Scientific, #C10045) and SPY650-DNA (1 μM for 1 h, Cytoskeleton, #CY-SC50) at 37 °C, 5% CO_2. Cells were spun down, resuspended in 150 μL of HBSS (Gibco, #14170112), and then seeded into 8-well chambered cover glass coated with polylysine (Fisher Scientific, #80824). For the mixed cell experiments, cells were treated similarly except stained with 1:50 dilution of CD36-APC (BD Bioscience, #550956) antibody instead of SPYDNA.

Spinning Disc Confocal and DIC Microscopy. Imaging was performed on a Nikon Eclipse Ti2 microscope equipped with Perfect Focus, an Okolab stage-top incubator, a Crest X-light V3 spinning disc scanhead, a Kinetix sCMOS camera, a Plan Apo 60× oil 1.4 NA DIC Nikon objective lens, and the appropriate DIC prisms in place. Illumination was provided on the Crest V3 by a 7-line solid-state Celesta Laser Unit, 1 W per channel (405 nm; 445 nm; 488 nm; 515 nm; 561 nm; 640 nm; and 730 nm power measurement is at the fiber output). DIC illumination was provided by an LED. Microscopes were equipped with the Nikon motorized stage with xy linear encoders and a closed-loop *Z*-axis Piezo nanopositioning system with 200 μm travel. Laser confocal or DIC illumination was selected with electronic shutters and an automated filter turret containing a multibandpass dichromatic mirror together with an electronic emission filterwheel. Microscope functions were controlled with NIS-Elements software (Nikon).

Stained cells on an 8-well chambered cover glass were placed on a prewarmed (37 °C) microscope stage. Sample temperature, humidity, and CO_2 levels were controlled with the Okolab stage top incubator. In each well, 2 to 3 random fields containing multiple cells were selected as central positions of a 3 × 3 tiling grid which was imaged with a 5% overlay and stitched using NIS element. Each position was imaged with the following settings (Excitation wavelength (laser power, exposure time): 405 nm (10%, 200 ms); 561 nm (1%, 250 ms); 488 nm (10%, 500 ms); 640 nm (3%, 500 ms). For the mixed cell samples, images were acquired at the cell-coverslip interface (to focus on Jurkat cells) and 1−3 μm above (to focus on HUDEP-2 cells).

Quantification of Confocal Images of Cellular Uptake. Images were processed with a home-built plugin that is compatible with imageJ plugins. The plugin created a cell mask based on the 561 nm channel (CellMask dye), a DNA mask based on the 640 nm channel (SPY650-DNA dye), and a dead cell mask based on the 405 nm channel (DAPI). It then extracted features with respect to each mask, such as cell area and mean fluorescence for channels of interest. The second customized python code calculated the background-corrected mean cell fluorescence of protein within each cell by first subtracting the cell-size adjusted background fluorescence from the cells' total fluorescence and dividing it by total cell area. The code then checked to ensure that each cell was positive for SPY650-DNA (contains a nucleus) but negative for DAPI (is not dead). Cells that did not meet either criterion were excluded (Figure S15). For Figures 4 and 7, this exclusionary processing only checked for and removed cells that were DAPI positive (dead cells), as cells were not treated with SPY650-DNA. CD36-APC (fluorescent for HUDEP-2 cells only) was used to identify cells under mixed cell conditions. Cells were clustered by using a Gaussian Mixture Model based on the 640 nm channel.

Flow Cytometry Experiments

Cells were treated as described above (see section on *Cellular uptake assay and viability studies*) with final concentration shown in results and figure, except that cells were immediately analyzed after treatment, without an additional recovery period. Following treatment, cells were washed three times with dPBS. To eliminate uninternalized recombinant proteins and aggregates from the cell membrane, cells were incubated with 0.05% trypsin at 37 °C for 7 min. Trypsin digest was inactivated by adding 5× media + 10% FBS. Samples with a single cell type were centrifuged (300 × *g* for 5 min) and resuspended in dPBS for immediate analysis. Samples from the mixed cell populations were incubated for an additional 1 h at 4 °C with CD36$^-$APC (BD Bioscience, #550956) and/or CD3-PECy7(BD Bioscience, #563423) antibodies at 1:50 and 1:62.5 volume dilutions, respectively. Cells were washed again twice with dPBS, and 5×10^4 or 1×10^5 cells were analyzed. To determine GPA expression of various cell types, 1×10^6 cells were washed with dPBS, incubated with a 1:100 dilution of CD235a-APC (BD Bioscience, #551336) for 1 h at 4 °C, washed twice with PBS, and analyzed. Cells were analyzed using a SONY Cell Sorter SH800S or BD AccuriTM C6 Plus.

Toxin Delivery Assay

PVC designs employed either the target-binding domain from human adenovirus 5 (producing Pvc13−Ad5knob) or IH4 nanobody (producing Pvc13−IH4) appended within accessory gene Pvc13 (replacing amino acids 403−476).[31] PVC and native toxin were copurified to make toxin-loaded PVCs. HUDEP-2, Jurkat, and HEK-293T cells were incubated with either dPBS, PVC-Ad5knob, or PVC-IH4 at 150 ng/μL for 24 h. Cell viability was assessed using the CellTiter-Glo 2.0 assay kit and presented as cytotoxicity normalized to control samples.

General Software

Microscopy pictures were processed with ImageJ including the FIJI package. Graphing and statistics determination were performed using Graphpad Prism 8. Flow cytometry data was processed and analyzed using FlowJo software (version 10.7.1; Tree Star, Inc., Ashland, OR, USA).

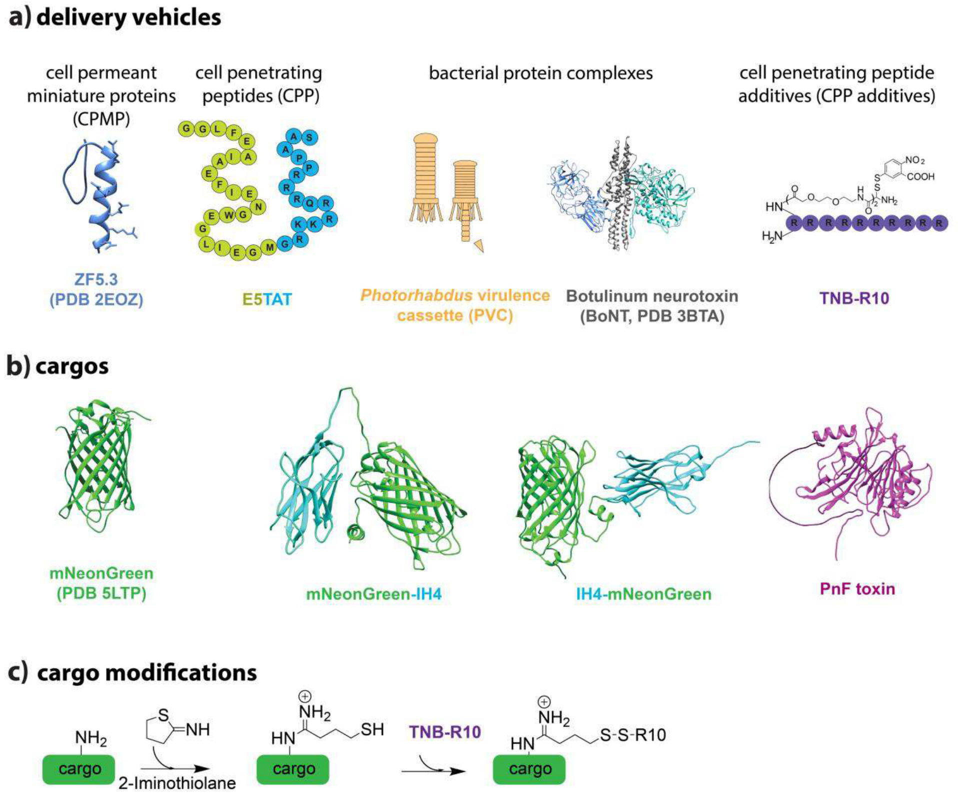

Figure 1. Schematic description of proteins used in this study. (**a**) Classes of protein DVs include CPMP (ZF5.3), CPP (E5TAT), CPP additive (TNB-R10), and bacterial toxins (PVC and BoNT). (**b**) Cargo proteins delivered by the DVs and (**c**) description of a modification to the cargo to improve TNB-R10 conjugation.

Statistics

All data reported were mean ± SEM. Statistical analysis represents p values obtained from one-way ANOVA or two-way ANOVA; ns, not significant; ****$p \leq 0.0001$, ***$p \leq 0.0002$, **$p \leq 0.0021$, *$p \leq 0.03$.

RESULTS

Choice of Delivery Vehicles (DVs) and Cargo

To investigate protein uptake in erythroid lineage cells, we tested several protein DVs that have been reported to successfully deliver functional proteins to the cytosol of the cells. Our vehicles included ZF5.3,[27,47] E5TAT,[24,28] and 5-thio-2-nitrobenzoic acid (TNB)-R10[45] (Figure 1a). ZF5.3 is a rationally engineered CPMP that leverages the specific dispersion of charge across the protein surface to deliver cargo via endocytosis.[40,47] The unstructured cell penetrating peptide (CPP) E5TAT is an amphipathic peptide that combines TAT (derived from HIV TAT protein) and E5, a pH-sensitive peptide derived from the influenza hemeagglutinin N-terminal peptide HA2. Due to its pH-dependent membrane binding and disruption E5TAT has been reported to show improved cytosolic delivery when compared to TAT.[24,28] Also included in the study is TNB-R10, a thiol-reactive CPP in which Cys-R10 peptide is conjugated to a reactive 5-thio-2-nitrobenzoic acid at the free cysteine. Thiol-reactive CPP additives like TNB-R10 leverage abundance in thiol on the cell surface to create nucleation zones for direct cellular penetrance.[45]

To assess each vehicle, we used mNeonGreen (mNG) as a model cargo (Figure 1b). mNG is a 26.6 kDa membrane impermeant green fluorescent protein that permits tracking of intracellular uptake using both confocal microscopy and flow cytometry. ZF5.3 and E5TAT were both appended to the N-terminus of mNG to make **ZF5.3-mNG** and **E5TAT-mNG** (Figure S1) while TNB-R10 (Figure S2) was incubated with mNG cargo and 5-thio-2-nitrobenzoic acid, which forms a covalent bond with accessible cysteines on mNG (Figures 1c, S1). Additionally, we investigated the benefit of molar excess TNBR-10 by comparing **mNG-1× TNB-R10** and **mNG-3× TNB-R10.** To improve surface decoration of protein cargo with TNB-R10, cargo was reacted with excess equivalents of 2-iminothiolane to convert surface lysines to amidine moieties with sulfhydryl groups (Figures 1c, S3). While other methods have used TNB-R10 in excess (20 equiv or more),[45] the cell lines used in this study showed sensitivity to large amounts of TNB-R10 and 2-iminothiolane (Figure S4). Quantification of accessible cysteines in the cargo showed that overall, low levels of free sulfydryls are available, even following modification with 2-iminothiolane. However, similar levels of TNB-R10 decoration were observed in both **mNG-1× TNB-R10** and **mNG-3× TNB-R10** conditions (Figure S3), as evidenced by the similar levels of sulfhydryls detected after incubation with the additive. This therefore suggests that the **3× TNB-R10** condition has unbound TNB-R10 that may function as an additive.

We also investigated bacterial toxin vehicles where a receptor targeting moiety is necessary for cargo delivery. Botulinum neurotoxin (BoNT)[30] and *Photorhabdus* virulence cassette extracellular contractile injection systems (PVC)[31] have recently been used for receptor-mediated delivery of active proteins (Figure 1a). Finally, these vehicles were tested side-by-side in erythroid precursors (represented by HUDEP-2 cells) and T-cells (represented by Jurkat cells). Because the two are relevant

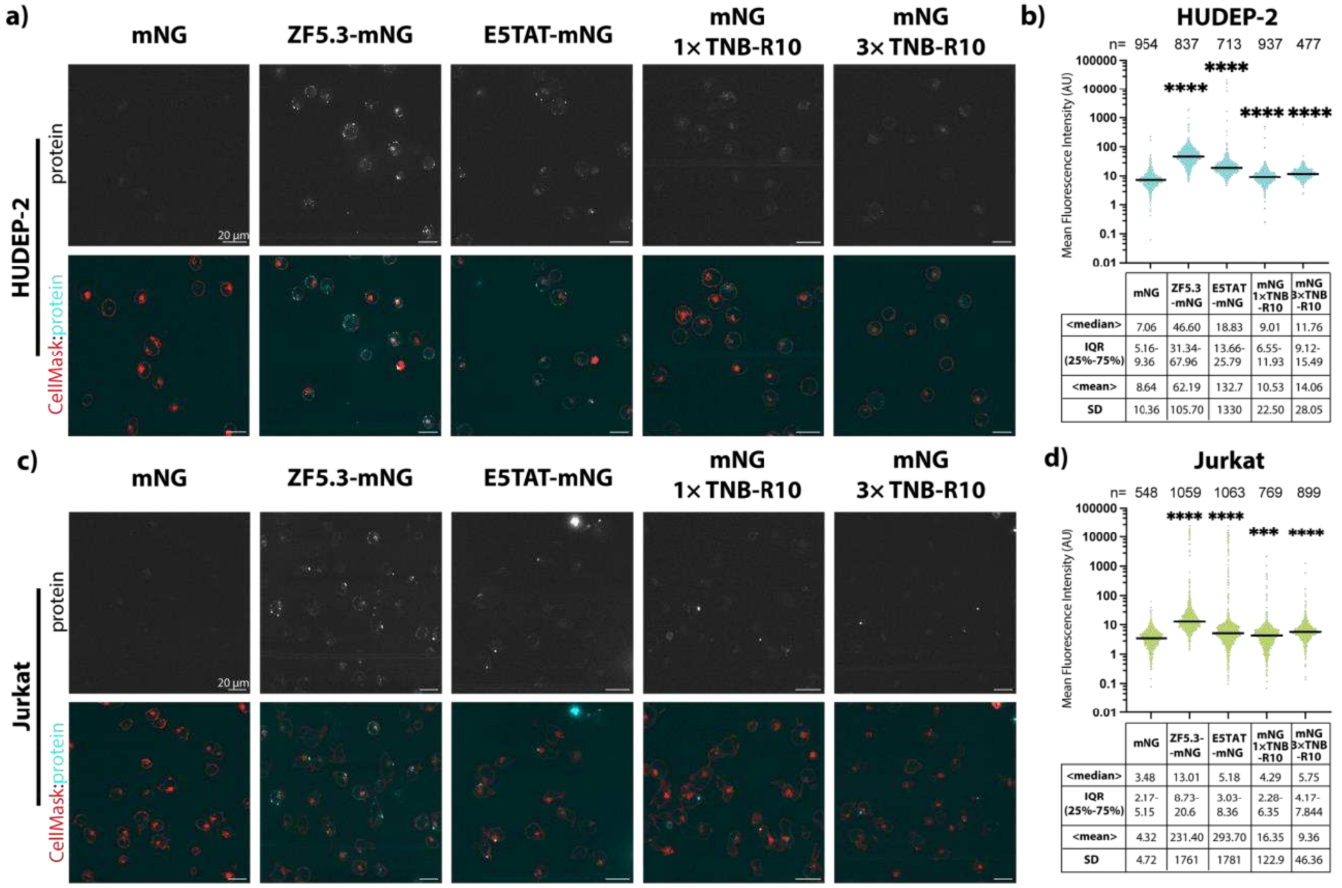

b) HUDEP-2

	mNG	ZF5.3 -mNG	E5TAT -mNG	mNG 1×TNB -R10	mNG 3×TNB -R10
<median>	7.06	46.60	18.83	9.01	11.76
IQR (25%-75%)	5.16-9.36	31.34-67.96	13.66-25.79	6.55-11.93	9.12-15.49
<mean>	8.64	62.19	132.7	10.53	14.06
SD	10.36	105.70	1330	22.50	28.05

d) Jurkat

	mNG	ZF5.3- -mNG	E5TAT -mNG	mNG 1×TNB -R10	mNG 3×TNB -R10
<median>	3.48	13.01	5.18	4.29	5.75
IQR (25%-75%)	2.17-5.15	8.73-20.6	3.03-8.36	2.28-6.35	4.17-7.844
<mean>	4.32	231.40	293.70	16.35	9.36
SD	4.72	1761	1781	122.9	46.36

Figure 2. Representative confocal microscopy images taken on a spinning disc confocal and DIC microscope of live **a**) HUDEP-2 and **c**) Jurkat cells treated with 8 μM of **ZF5.3-mNG, mNG-1 × TNB-R10, mNG-3× TNB-R10,** or **E5TAT-mNG** for 1 h, recovered for an additional 1 h. Protein is first shown in gray and then shown in cyan overlapped with cell mask (red). Quantification of mean fluorescence intensity (total fluorescence intensity was background corrected and normalized to cell area) from confocal images of HUDEP-2 (b) and Jurkat cells (d). Median fluorescence intensity from (**b**) and (**d**) are represented with black bars and descriptive statistics are shown for each condition. n represents the number of cells quantified per condition. *P*-values were determined by one-way analysis of variance (ANOVA) followed by Kruskal−Wallis and Mann−Whitney tests and compared to mNG only treatment. Scale bar = 20 μm.

model systems, a comparison of their uptake efficiencies can reveal whether the vehicles have any inherent cell-type differences.

Each of these vehicles has been shown in previous reports to have robust cytosolic delivery. This work focused on using quantitative live confocal microscopy and flow cytometry methods to (i) determine and compare overall uptake of protein cargo into developing erythrocytes and T-cells models and (ii) investigate the amenability of each DV to protein engineering methods that improve their selectivity and potency. These two orthogonal techniques allow for the probing of multiple aspects of uptake. Our live cell confocal techniques provide high-resolution images that can determine cargo localization within a cell and reveal uptake variability within a population of living cells. This is supplemented with flow cytometry, which allows a high-throughput analysis of cell populations to determine the impact of cargo concentration and treatment conditions.

Delivery Efficiency Varies across Cell Type and Delivery Vehicle

To evaluate protein delivery in live cells, we performed high-resolution live confocal imaging using spinning disk confocal microscopy. Because many protein-based delivery vehicles are operant at μM concentrations,[40,47] HUDEP-2 and Jurkat cells were treated with 8 μM of unmodified mNG only (control) or mNG-DV for 1 h in unenriched media (media without any supplements). The cells were then stained with CellMask to visualize the plasma membrane, SPY650-DNA to visualize the nuclear DNA, and DAPI to label the DNA of the dead cells. Visualization of the confocal images of more than 1000 HUDEP-2 and Jurkat cells showed that the intracellular signal of mNG increases in all cells treated with protein fused or conjugated to the DVs.[48] Cells treated with **ZF5.3-mNG** and **E5TAT-mNG** showed strong, puncti signals while those treated with **mNG-1× TNB-R10** and **mNG-3× TNB-R10** displayed more diffused fluorescence (Figure 2a,c). Both **ZF5.3-mNG** and **E5TAT-mNG** displayed overlap of mNG signal with that of lysotracker-RED, suggesting that the cargo remained entrapped in the late endosomes or lysosomes at the time of imaging (Figure S7). Because our goal was to understand cell uptake, we did not pursue additional investigation of this observation.[24,30] To quantify the variability in delivery efficiency as a function of the delivery vehicle, we developed a python-based automatic image analysis pipeline that uses the CellMask signal (plasma membrane) to segment single cells and calculate the mean background-subtracted mNG fluorescence signal in thousands of single HUDEP-2 and Jurkat cells, one at a time (Figure 2b,d).

The quantification of confocal images allows us to examine the total uptake as well as variability in delivery efficiency at the population level. A striking result is the heterogeneity of uptake observed between cell types and delivery vehicles (Figure 2). We found that in both cell types, vehicles **ZF5.3-mNG** and **E5TAT-mNG** display 5−66× greater heterogeneity in mNG signal (as defined by standard deviation of the distribution of mean fluorescence intensity of mNG) than with vehicles **mNG-3× TNB-R10** and **mNG-1× TNB-R10**. When comparing cell types, we observed that Jurkat cells showed 2−16× greater heterogeneity in the mNG signal across all vehicles when compared to HUDEP-2 cells but particularly with **ZF5.3-mNG** and **E5TAT-mNG**. This indicates that uptake with **ZF5.3-mNG** and **E5TAT-mNG** is more variable within a given cell population but also more variable when comparing the two cell types. Due to the heterogeneity in uptake/delivery efficiency between vehicles, we used the median of the distributions of mNG fluorescence signal to compare the efficiency of uptake/delivery between Jurkat and HUDEP-2 cells.

Quantification of the intracellular signal between delivery vehicles showed that compared to control, all vehicles display significant cargo uptake in the two cell types (Figure 2c,d). In these conditions, ZF5.3 is the most efficient DV with a median fluorescent intensity that is either 2.5−5 × greater (HUDEP-2) or 2.5−3× greater (Jurkat) than is observed with the other vehicles. Interestingly, despite the low fluorescence signal visualized by eye in cells treated with **mNG-1× TNB-R10** and **mNG-3× TNB-R10** (Figure 2a,c), quantitative analysis revealed significant uptake when compared to the mNG-only cells (Figure 2b,d). This can be rationalized by the diffuse nature of the fluorescence across the full cells rather than the concentration of the signal in a compartment. The quantification also showed slightly more uptake (1.3−1.4 ×) with **mNG-3× TNB-R10** than **mNG-1× TNB-R10**. Given that the quantification of free cysteines suggests equivalent TNB-R10 labeling of the proteins, the slightly higher uptake of **mNG-3× TNB-R10** might be a consequence of excess TNB-R10 acting as an additive (Figure 2b,d).

To further define the delivery efficiencies across delivery vehicles and to compare uptake efficiencies between cell types, we used flow cytometry to measure the dose response of mNG uptake (Figures 3a, S6). While high-resolution confocal microscopy allows us to access subcellular localization of proteins, it can only assess a limited number of cells; flow cytometry allows analysis of many more cells at the same time and can allow rapid testing of a variety of conditions. For these experiments, cells were treated with protein concentrations that ranged from 0.1 to 8 μM for 1 h and washed immediately before measurement. This range of concentrations permits a determination of the minimum concentration at which each DV mediates the cargo uptake. To ensure only intracellular protein signal was detected, cells were incubated for 7 min with 0.05% trypsin to digest nonspecific surface-bound mNG-vehicle or aggregates. To draw comparisons across doses, cell types, and vehicles, values are reported as the fold change of median fluorescence intensity (MFI) of treated versus untreated cells (control). Consistent with our confocal microscopy-based analysis, all vehicles showed significant uptake (defined here as at least 1.5× increase in the MFI compared to control), indicating they are sufficient for cargo delivery into HUDEP-2 and Jurkat cells. Some vehicles, such as **ZF5.3-mNG** and **E5TAT-mNG**, mediated significant uptake in both cell types at 0.4 μM while **mNG-1× TNB-R10** and **mNG-3× TNB-R10** did not achieve this until 1 μM (Figure 3b-g). As observed with the microscopy data, **ZF5.3-mNG** was the most efficient delivery vehicle, as evidenced by the 2−4× higher fluorescence detected in cells treated with this construct (Figure 3b,c). However, the flow cytometry data revealed that **ZF5.3-mNG** and **E5TAT-mNG** have markedly different efficiencies in the two cell types used, with both vehicles displaying greater uptake in Jurkat cells than in HUDEP-2 cells (Figure 3d,e). For **ZF5.3-mNG**, the difference in uptake in the two cell types is significantly different at concentrations as low as 2 μM, whereas this happens at 8 μM for **E5TAT-mNG**. Finally, while the microscopy experiments showed that **mNG-3× TNB-R10** was slightly better at uptake compared with **mNG-1× TNB-R10**, the flow cytometry data (which represents a much greater population than the microscopy experiments) revealed that the difference between these vehicles is not statistically significant (Figure 3f,g).

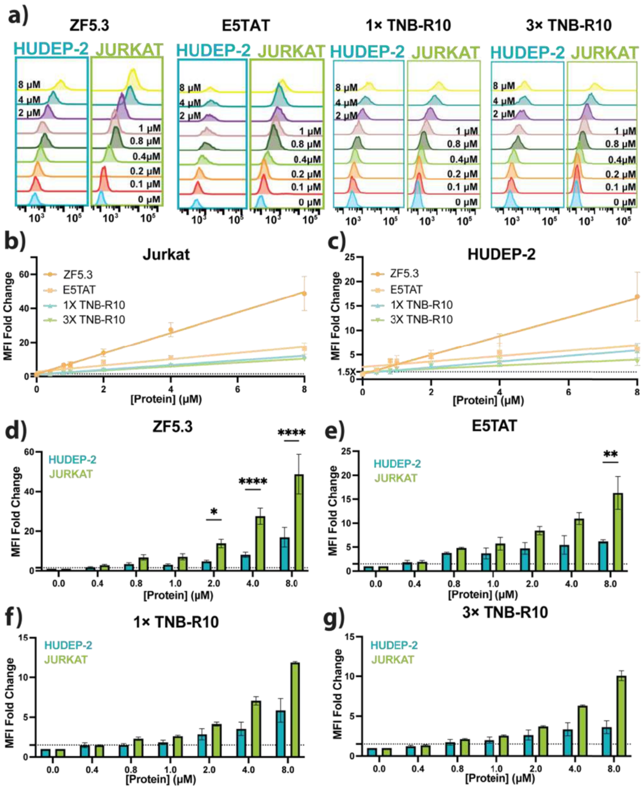

Figure 3. Dose-dependent delivery of mNG by the different DVs. Uptake of mNG in HUDEP-2 and Jurkat cells; cells were treated for 1 h, washed, and incubated with trypsin to remove surface proteins and quantified by flow cytometry. **a)** Repersenative histograms of each sample. **b-g)** Data shown as fold change of median fluorescence intensity (MFI) values compared to untreated cells. **b,c)** MFI fold change data points were fit using a simple linear regression (Table S5). **d-g)** MFI fold change shown as bar graph representation of the data with a dashed horizontal line indicating the point of significant uptake (MFI >1.5×, compared to untreated samples). MFI values corresponding to each mNG-vehicle were compared to nontreated cells and between cell types at each dose, and *P*-values were determined by two-way analysis of variance (ANOVA) of *N* = 3 biological replicates.

Targeting to HUDEP-2 Cells Using GYPA

Because of the lower cargo uptake efficiency in HUDEP-2 cells (Figure 3), we attempted to increase the potency of DVs by engineering vehicles with increased affinity to the cell surface. By appending a ligand to an erythroid-specific cell surface receptor, we hypothesized that the ligand would increase surface binding of the entire construct and therefore increase local concentration and probability of uptake. We sought receptors that were (i) highly expressed and therefore abundant on the cell surface, (ii) uniquely expressed on erythroid lineage, and (iii) had ligands that could be readily appended to our existing vehicles. During erythropoiesis, developing erythrocytes express several major receptors.[49,50] Notably, the transferrin receptor (CD71) controls the import of iron into cells;[51] erythropoietin receptor (EPOR) binds erythropoietin and signals the production of new red blood cells;[52] and GYPA serves as antigenic marker of blood cell types and maintains membrane integrity[41,53] (Figure S8). Of these three, GYPA is abundant with an estimated ∼50,000 copies/cell.[53] Moreover, it is exclusively expressed on erythroid lineage cells and is irrelevant for red blood cell maturation or signaling, which allows it to be targeted without concern of impacting the metabolism or proteome directly (Figure S9). Previous work identified IH4 as a high-affinity nanobody ligand for GYPA with a K_d of 33 nM. Because IH4 was used to target biomolecules successfully to the erythrocyte surface,[54] we suspected it would be beneficial for directing intracellular delivery vehicles to erythroid cells.

To confirm that GYPA was indeed specific to erythroid lineage cells, cells were incubated with anti-GYPA fluorescent antibody, washed extensively, and then analyzed using flow cytometry. Based on the measured fluorescence signal, the surface expression of GYPA was determined to be 197× more in HUDEP-2 cells than in Jurkat cells (Figure 4a). Flow cytometry was also used to determine the relative binding affinity of IH4 fusion proteins for the surface of each cell type. IH4 was appended to the N-terminus of mNG to create **IH4-mNG** (Figure 1b), which was incubated with the cells for 1 h at 37 °C. Surprisingly, the IH4 fusion constructs only afforded a 2× increase in affinity to HUDEP-2 cell surface over Jurkat cells, while mNG alone showed similar surface affinity for both cell types (Figure 4b).

Despite the IH4-containing constructs showing only a modest improvement in affinity for HUDEP-2, we moved forward to determine whether IH4 could be used to direct vehicles into the erythroid precursor cells. For these experiments, we preferred TNB-R10 as the vehicle because of the diffuse fluorescent signal that suggests that the protein is not concentrated in a particular subcellular location (see Figure 2). Moreover, the low levels of uptake observed with this vehicle suggest that cargo uptake can be increased with a lower risk of saturating the signal. Because the flow cytometry data suggested that 1 μM is the minimum concentration needed to observe uptake of **mNG-3× TNB-R10** into both cell types, this concentration was used for treatment with **mNG-3× TNB-R10** and **IH4-mNG-3× TNB-R10** (not modified with 2-iminothiolane). It is noteworthy that the unmodified cargo has no surface-accessible cysteines (Figure S3), which ensures that TNB-R10 acts solely as an additive to permeabilize the cell. We also engineered and tested **mNG-IH4-3× TNB-R10**, where IH4 was appended at the C-terminus; this produced a result similar to those obtained with **IH4-mNG-3× TNB-R10**, but the protein was less stable. HUDEP-2 and Jurkat cells were treated for 2 h with 1 μM fusion proteins in enriched media and then imaged using live-cell confocal microscopy (Figure 4c-f). Representative images and quantification of **IH4-mNG-3× TNB-R10** showed greater mNG fluorescence in HUDEP-2 cells when compared to Jurkat cells (Figure 4c,e). In HUDEP-2 cells, **IH4-mNG-3× TNB-R10** showed 4.5 × and 2× greater mean and median fluorescence intensity, respectively, than **mNG-3× TNB-R10**, while in Jurkat cells, **IH4-mNG-3× TNB-R10** only showed 1.65 × and 1.4 × increase in mean and median fluorescence intensity, respectively (Figure 4d,f). This result shows that despite the weak affinity for HUDEP-2 cells, IH4 can be used to direct cargo into cells expressing GYPA.

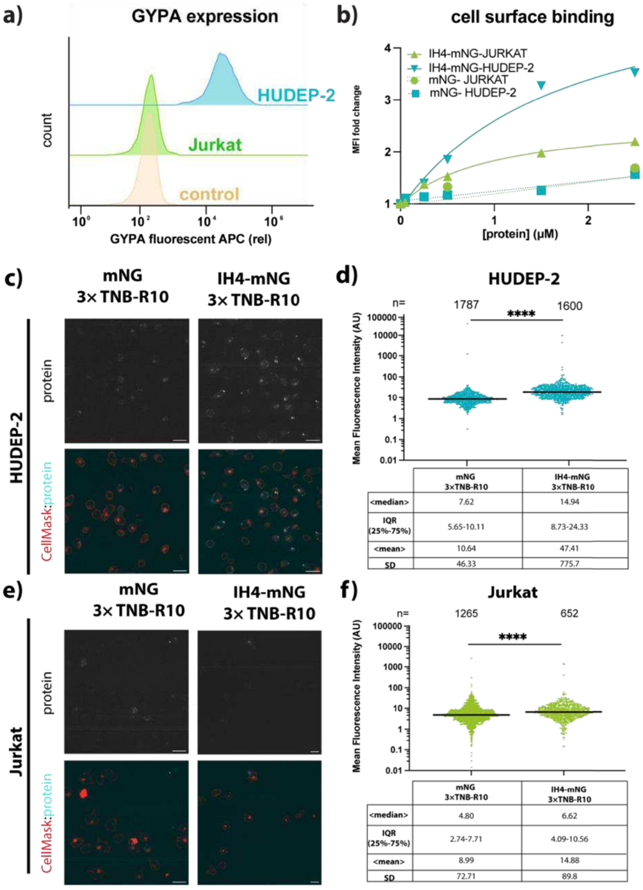

Figure 4. Engineering cell-specific DVs. **a**) Flow cytometry analysis of GYPA levels on the surface of HUDEP-2 and Jurkat cells. **b**) Surface binding of proteins to HUDEP-2 and Jurkat cells. Cells were treated with 0−2.5 μM of protein and analyzed using flow cytometry. Data is shown as fold change of MFI values compared to untreated cells. **c, e**) Representative confocal microscopy images of live HUDEP-2 (**c**) and Jurkat cells (**e**) taken on spinning disc confocal and DIC microscope; cells were treated with 1 μM of **mNG-1 × TNB-R10** or **IH4-mNG-3× TNB-R10** unmodified with 2-iminiothiolane for 2 h. Protein is first shown in gray and then shown in cyan overlapped with cell mask (red). **e, f**) Quantification of mean fluorescence intensity from confocal images of HUDEP-2 (**e**) and Jurkat cells (**f**). Median is represented with a black bar, and descriptive statistics are shown for each condition. N represents the number of cells quantified per image. *P*-values were determined by one-way analysis of variance (ANOVA) followed by Kruskal−Wallis test and compared to treatment of mNG only of three biological replicates.

IH4 Addition Increases Uptake Only with Certain Vehicles

To determine whether IH4 fusions can be generalized to improve intracellular delivery across various vehicles, we revisited the two best-performing vehicles identified so far (ZF5.3 and E5TAT). In this instance, we also considered whether the uptake enhancement occurs at high concentrations of these vehicles. By fusing IH4 to the two vehicles, we created **E5TAT-mNG-IH4** and **ZF5.3-mNG-IH4**. To ensure a direct comparison with TNBR10, we included **IH4-mNG-1× TNB-R10** and **IH4-mNG-3× TNB-R10** (modified with 5 equiv of 2-iminiothiolane). Because appending IH4 to **E5TAT-mNG**

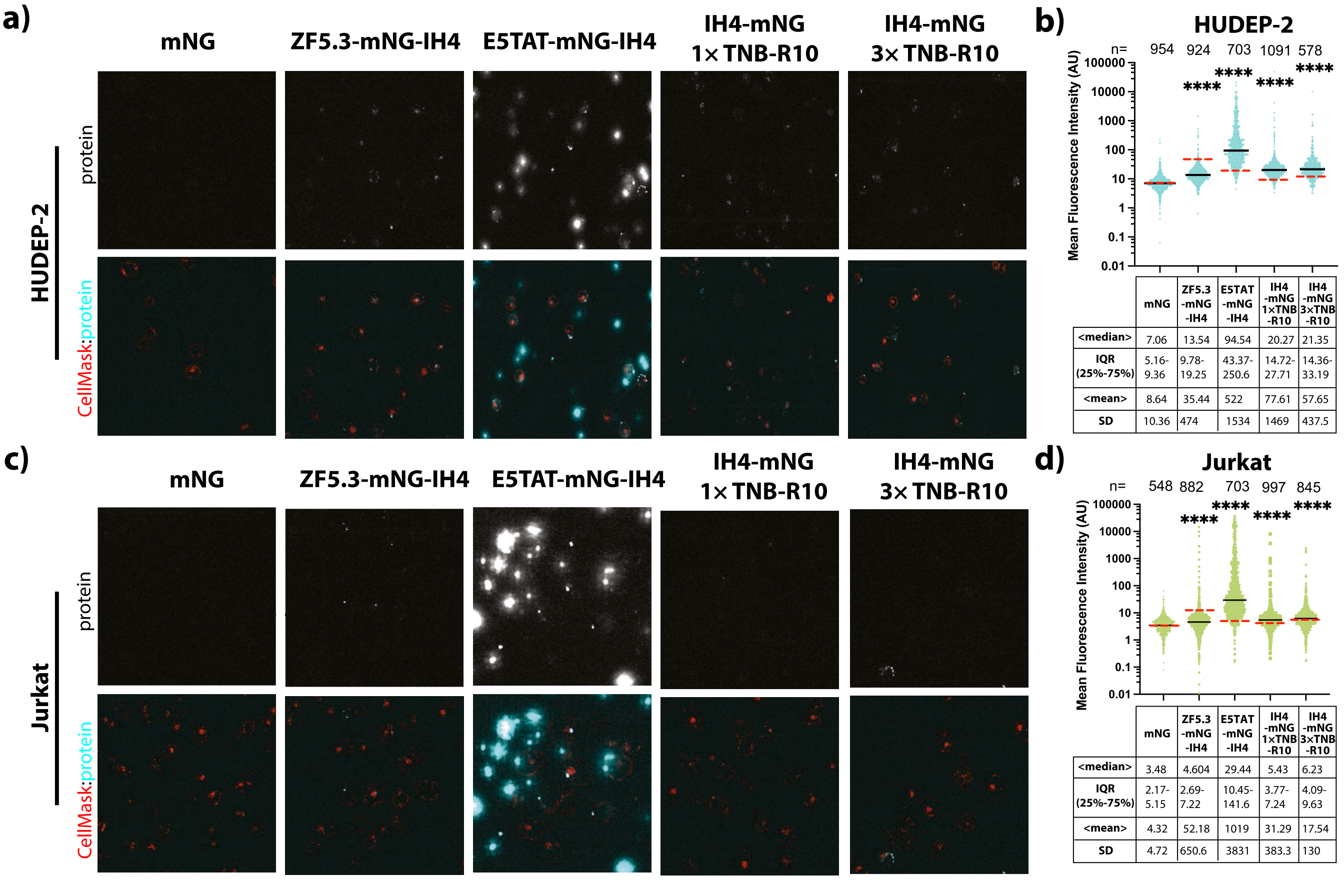

b) HUDEP-2

	mNG	ZF5.3 -mNG -IH4	E5TAT -mNG -IH4	IH4 -mNG 1×TNB -R10	IH4 -mNG 3×TNB -R10
<median>	7.06	13.54	94.54	20.27	21.35
IQR (25%-75%)	5.16-9.36	9.78-19.25	43.37-250.6	14.72-27.71	14.36-33.19
<mean>	8.64	35.44	522	77.61	57.65
SD	10.36	474	1534	1469	437.5

d) Jurkat

	mNG	ZF5.3 -mNG -IH4	E5TAT -mNG -IH4	IH4 -mNG 1×TNB -R10	IH4 -mNG 3×TNB -R10
<median>	3.48	4.604	29.44	5.43	6.23
IQR (25%-75%)	2.17-5.15	2.69-7.22	10.45-141.6	3.77-7.24	4.09-9.63
<mean>	4.32	52.18	1019	31.29	17.54
SD	4.72	650.6	3831	383.3	130

Figure 5. Representative confocal microscopy images of live **a**) HUDEP-2 and **c**) Jurkat cells taken on spinning disc confocal and DIC microscope. Cells were treated with 5 μM **ZF5.3-mNG-IH4**, **E5TAT-mNG-IH4**, **IH4-mNG-1 × -TNB-R10**, and **IH4-mNG-3 × -TNB-R10** for 1 h, recovered for an additional 1 h before imaging. Black bars correspond to the median of each treatment (DV-IH4), and red dashed lines correspond to the median of the DV without IH4 (from Figure 2). The protein is first shown in gray and then shown in cyan overlapped with cell mask (red). Quantification of mean fluorescence intensity for confocal images from of HUDEP-2 (**b**) and Jurkat cells (**d**). Median is represented with a black bar, and descriptive statistics are shown for each condition. n represents the number of cells quantified per image. P-values were determined by one-way analysis of variance (ANOVA) followed by Kruskal−Wallis and Mann−Whitney tests and compared to mNG only treatment of two biological replicates. Scale bar = 20 μm.

resulted in protein instability, all vehicles were tested using 5 μM cargo added to cells for 1 h. Live cell confocal microscopy imaging revealed mNG signal in cells treated with all DVs, with HUDEP-2 cells containing greater fluorescence signal than Jurkat cells for all vehicles except E5TAT. While **E5TAT-mNG** had the highest signal, most of the signal arose from extracellular aggregation that was difficult to exclude during quantification (Figure 5a,c). Quantification of the fluorescence signal revealed a notable decrease in overall signal in cells treated with **ZF5.3-mNG-IH4** when compared to **ZF5.3-mNG** (median fluorescence intensity from Figure 2 indicated by a red dashed line). This finding hints that IH4 *lowered* the efficiency of ZF5.3. We also observed a 4−7× increased uptake in HUDEP-2 cells treated with **IH4-mNG-1× TNB-R10** and **IH4-mNG-3× TNB-R10**; this value was only 1.9× in Jurkat cells treated with the same constructs (Figure 5b,d). This result is consistent with the findings of experiments that used a lower concentration of these vehicles (reported in Figure 4c-f). Together, the data indicate that use of IH4 with **TNB-R10** but not with ZF5.3 or E5TAT increased the cargo in HUDEP-2 cells specifically.

To further determine whether IH4 fusions can be used to improve the intracellular delivery of various vehicles, we performed similar experiments using vehicles where a receptor targeting moiety is necessary for functional delivery. Botulinum neurotoxin (BoNT)[30] and *Photorhabdus* virulence cassette extracellular contractile injection systems (PVC)[31] have recently been used for receptor-mediated delivery of active proteins (Figure 1a). BoNTs have three domains: a receptor binding domain that enables receptor-mediated endocytosis, a translocation domain for escape from endosomes through pore formation, and an endogenous protease that is connected through a labile disulfide bond.[55] PVCs are self-assembling nano syringe-like structures that bind to cells and inject protein payloads by driving a spike through the cellular membrane.[31,56] Previously, both BoNT and PVC systems were repurposed to direct intracellular delivery with various receptor-targeting ligands (nanobodies, DARPin, epitope tags, etc.). To determine whether these vehicles were conducive for protein delivery into erythroid precursor cells, we developed fusions that replaced their targeting domains with IH4. For BoNT, IH4 was appended to the C-terminus translocation domain and mNG added to the N-terminus of the inactivated protease to yield construct **mNG-BoNT-IH4**. For the PVC, IH4 was placed within the tail fiber gene (pvc13) to yield **PVC-pvc13IH4**. The concentrations and treatment time of these DVs were adjusted to match those used in published reports (~200 nM for 24 h), which is lower than what is routine for CPP/CPMP vehicles (1−10 μM for 1−4 h).

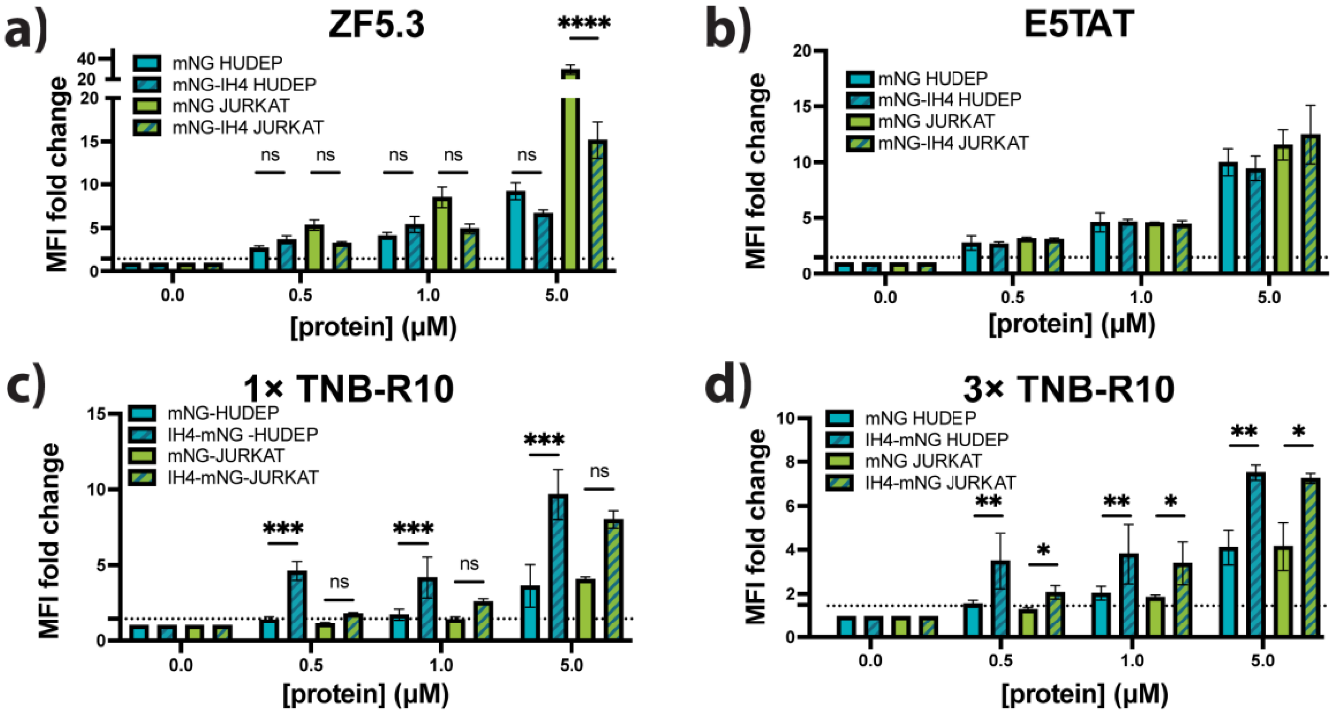

Figure 6. Comparison of uptake by DVs with and without targeting ligand IH4 appended assessed by flow cytomtery. (**a-d**) Dose-dependent fluorescence in cells treated with varying concentrations of proteins and DVs. Cells were treated with either 0.5, 1, or 5 μM **ZF5.3-mNG-IH4, E5TAT-mNG-IH4, IH4-mNG-1 × -TNB-R10**, and **IH4-mNG-3 × -TNB-R10**. Data is shown as fold change of MFI values compared to untreated cells and represents the fluorescence intensity of cells. A dashed line at 1.5× fold change defined as significant uptake compared to untreated cells. MFI values corresponding to each mNG-vehicle were compared to nontreated cells and between cell types at each dose. *P*-values were determined by two-way analysis of variance (ANOVA) of three biological replicates.

Treating HUDEP and Jurkat cultures with 200 nM **mNG-BoNT-IH4** for 24 h and analyzing uptake using confocal microscopy imaging revealed no significant uptake of **mNG-BoNT-IH4** constructs in HUDEP-2 when compared to Jurkat cells and the control (**mNG-BoNT**) (Figure S10). Similarly, flow cytometry analysis of BoNT treatment resulted in no increase in intracellular mNG compared to the **mNG-BoNT** control or untreated cells (Figure S11). The lack of significant uptake by HUDEP-2 cells may be explained in part by low endocytic cycling of GYPA, as BoNT relies on receptor-mediated endocytosis and escape to deliver cargo. It is possible that a receptor that cycles more efficiently through the endocytic pathway would be ideal for use with BoNT.

Considering that loading cargo for PVC delivery requires very specific molecular interaction and assembly of payload into the injection system, we first sought to deliver native payload Pdptoxin payload Pnf, which is a highly active toxin (Figure 1b). As a positive control, we also produced **PVC-pvc13Ad5-Pnf** that leveraged the highly expressed Ad5 receptor and was reported to efficiently deliver toxin in HEK 293T. Briefly, HUDEP-2, Jurkat, and HEK 293T cells were treated for 24 h with either 150 ng/mL of purified **PVC-pvc13IH4-Pnf** or **PVC-pvc13Ad5-Pnf** and analyzed using a CellTiter-Glo 2.0 Cell viability assay.[31] Cells treated with the control **PVC-pvc13Ad5-Pnf** demonstrated nearly complete cytotoxicity of HEK293T cells but showed 5% cytotoxicity with HUDEP-2 and about 40% in Jurkat cells; Jurkat cells express low levels of CAR (the Ad5 Knob ligand receptor). However, treatment with **PVC-pvc13IH4-Pdp1-PnF** showed only 15% toxicity in HUDEP-2 cells; this value is similar to the toxicity measured in Jurkat and HEK293T cells (Figure S12). This data suggest that use of IH4 with PVC is not sufficient to allow protein delivery to cells expressing GYPA. Similar attempts to deliver green fluorescent protein (GFP) with **PVC-pvc13IH4** were not successful (data not shown). While the promise of PVC for intracellular delivery is exciting, significant optimization in construct design is necessary for nonmodel cell types. It is also possible that PVC delivers protein amounts that are below our detection limit.

Finally, to additionally quantify the impact of appending IH4 to the delivery vehicles described above, we performed flow cytometry experiments. HUDEP-2 and Jurkat cells were treated with a range of concentrations (0.5−5 μM) of either **mNG-vehicle** or **IH4-mNG-vehicle** for 1 h. Following treatment, the cells were washed, surface proteins were digested with trypsin, and samples were analyzed using flow cytometry (Figure 6a-d). Similar to the quantification from the microscopy images, the addition of IH4 to **ZF5.3** decreased the uptake in Jurkat cells at all concentrations tested. In HUDEP-2 cells, no change is observed at 0.5 and 1 μM, but a decrease in uptake is noticeable at 5 μM (Figure 6a). With **E5TAT-mNG- IH4**, no change in uptake was detected when compared to **E5TAT-mNG** (Figures 6c). Finally, a comparison of **IH4-mNG-1× TNB-R10** and **IH4-mNG-3× TNB-R10** to **mNG-1× TNB-R10** and **mNG-3× TNB-R10** showed that the IH4-containing constructs displayed a significant improvement in cargo uptake by HUDEP-2 cells (Figures 6c,d). For both the **1× TNB-R10** and **3× TNB-R10** treatments, we detected a 2-to-4× increase in uptake by HUDEP-2 cells at concentrations of 0.5 and 1 μM, while the same protein treatments did not show significant increase in Jurkat cells at those concentrations. At higher concentrations, an increased uptake in Jurkat cells was observed. Generally, IH4 addition to cargo with **1× TNB-R10** and **3× TNB-R10**

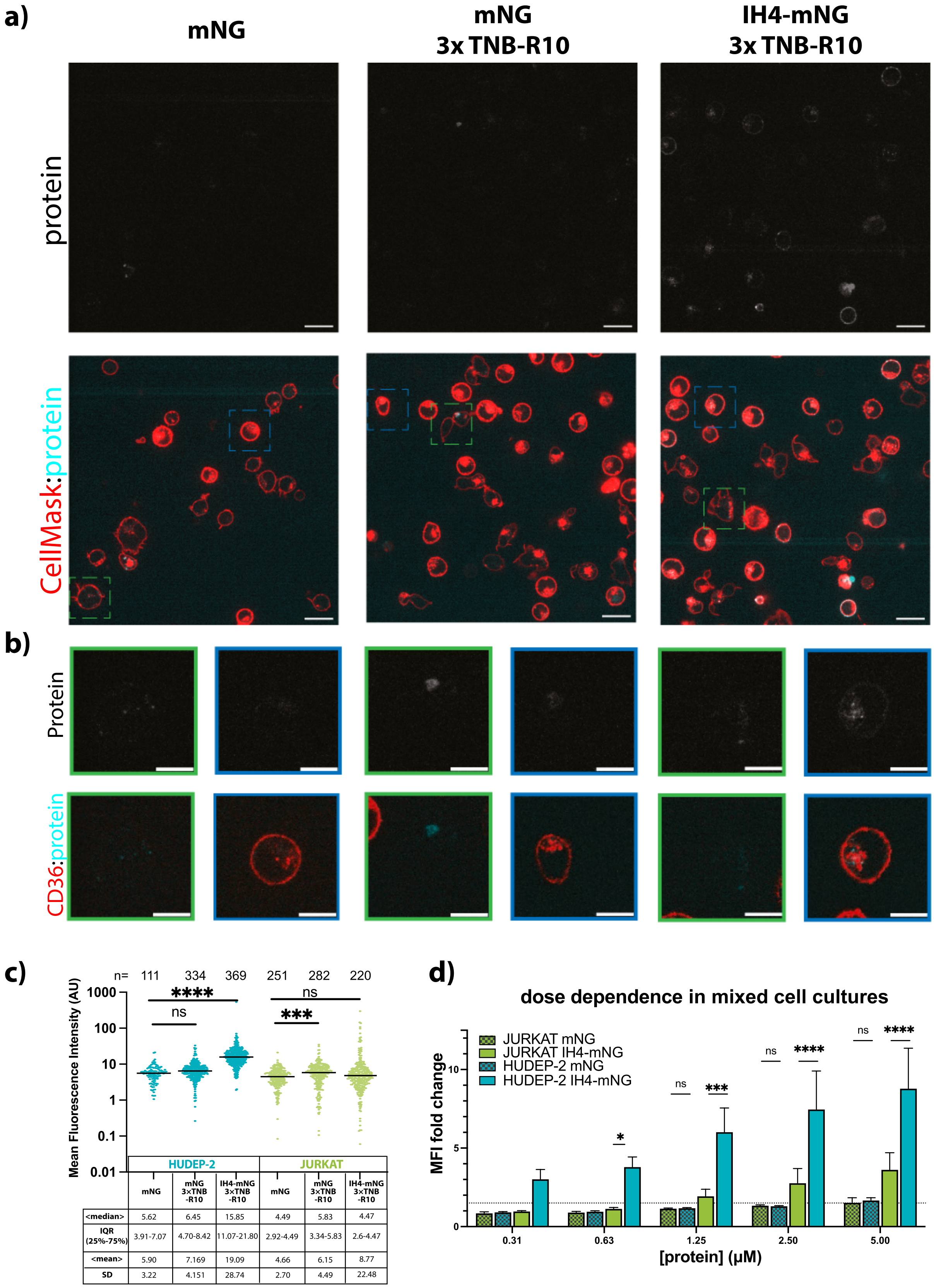

	HUDEP-2			JURKAT		
	mNG	mNG 3×TNB -R10	IH4-mNG 3×TNB -R10	mNG	mNG 3×TNB -R10	IH4-mNG 3×TNB -R10
<median>	5.62	6.45	15.85	4.49	5.83	4.47
IQR (25%-75%)	3.91-7.07	4.70-8.42	11.07-21.80	2.92-4.49	3.34-5.83	2.6-4.47
<mean>	5.90	7.169	19.09	4.66	6.15	8.77
SD	3.22	4.151	28.74	2.70	4.49	22.48

Figure 7. (**a**, **b**) Representative confocal microscopy images of mixed coculture of live HUDEP-2 and Jurkat cells taken on a spinning disc confocal and DIC microscope; cells were treated with 1 μM **mNG**, **mNG-3 × TNB-R10**, **IH4-mNG-3× TNB-R10** for 2 h, washed, and labeled with CD36-APC. Protein is first shown in gray and then shown in cyan overlapped with cell mask (red). (**c**) Quantification of mean fluorescence intensity for confocal images from **a**,**b** (background corrected and normalized to cell area). Gaussian Mixture Model was used to distinguish cells based on CD36-APC signal with CD36+ (HUDEP-2) and CD36− (Jurkat) which is positive for HUDEP-2 cells only (Figure S15). Median is represented with a black bar, and descriptive statistics are shown for each condition. N represents the number of cells quantified per image. P-values were determined by one-way

Figure 7. continued

analysis of variance (ANOVA) followed by Kruskal−Wallis and Mann−Whitney tests and compared to mNG only treatment of two biological replicates. Scale bar = 20 μm. **(d) mNG**, **mNG-3 × -TNBR-10**, or **IH4-mNG-3× TNB-R10** at 0.3 to 5 μM were added to cells for 2 h, washed to remove surface-bound proteins, labeled with CD36-APC and CD3-PE-Cy7 antibodies, and analyzed via flow cytometry. Gates were chosen stringently as HUDEP-2 (APC+PE-Cy-7−) and Jurkat (APC-PE-Cy-7+) as described in Figure S13. Data shown as MFI fold change of treated cells compared to mNG only treated cells. *P*-values were determined by two-way analysis of variance (ANOVA) of three biological replicates.

improved the cargo delivery to HUDEP-2 cells more than to Jurkat cells. A similar trend of slightly improved uptake for **1× TNB-R10** versus **3× TNB-R10** was also observed with their IH4 fusions affinity to the respective cell type surface. Therefore, the CPP additive TNB-R10 synergizes well with ligands that direct cargo to the cell surface.

Selective Uptake into HUDEP-2 in Mixed Cell Cultures

To probe the significance of the observed improved uptake of IH4 fusions with TNB-R10 into HUDEP-2 cells, we performed the delivery experiment in cultures containing both HUDEP-2 and Jurkat cells. We posited that if the improved uptake trends from single populations were due to specific interaction of IH4 with GYPA, this would enable specificity for HUPEP-2 cells when in a heterogeneous culture. Samples containing 1:1 HUDEP-2 and Jurkat cells were treated with 1 μM of either **IH4-mNG-3× TNB-R10**, **mNG-3× TNB-R10**, or **mNG** for 2 h at 37 °C. Cells were then washed and analyzed via live cell confocal microscopy. The mixed cell samples were also treated with the fluorescent antibody specific for CD36, a glycoprotein expressed on HUDEP-2 cells that is absent in Jurkat cells (Figure 7a,b). Quantification of the intracellular fluorescence showed a 3.5× increase in median uptake in CD36$^+$ cells when compared to CD36$^-$ cells when the mixed population was treated with **IH4-mNG-3× TNB-R10**; this value was only a 1.1× change when mixed cells were treated with **mNG-3× TNB-R10** (Figure 6b). In HUDEP-2 cells, the fluorescent protein signal was observed in subcellular compartments or diffuse throughout the cell and at the membrane. For Jurkat cells, very little diffuse signal was detected.

This finding was further validated using flow cytometry, which also permitted determination of the concentrations required to achieve this selectivity. Previous experiments with single cell populations showed that the selectivity of IH4 for HUDEP-2 cells decreases at higher concentrations of the treatment. We therefore treated the cell mixture with various concentrations of **IH4-mNG-3× TNB-R10**, **mNG-3× TNB-R10**, and **mNG** (ranging from 30 nM to 5 μM) and measured the fluorescence within each cell type (Figures 7c). Whereas in experiments with IH4 we determined that 0.4 μM was the minimum concentration of protein needed to observe significant cargo uptake, we explored lower concentrations in this experiment to investigate whether the IH4 targeting effect would result in a different phenomenon. CD36-APC was again used as a marker for HUDEP-2 cells with a fluorescent CD3-PECy7. Cells were stringently gated so that only CD36$^+$ /CD3$^-$ cells were labeled as HUDEP-2 cells and CD36$^-$/CD3$^+$ were labeled as Jurkat cells (Figure S13). Significant uptake (as before, this is defined as conditions resulting in 1.5× or greater MFI compared to vehicle treatment) of IH4-containing constructs in HUDEP-2 cells is observed at the much lower concentration of 310 nM. For Jurkat cells, significant uptake is observed at 1.25 μM, which agrees with the results from experiments with single cells. Furthermore, we consistently observed a 2.5−3 × fold higher uptake in HUDEP-2 cells over Jurkat cells with **IH4-mNG-3× TNB-R10**, while no such difference is apparent when IH4 is absent. Together, these data suggest that IH4, when used with the CPP additive TNB-R10, is sufficient to afford selectivity for HUDEP-2 cells in a heterogeneous population.

DISCUSSION

Delivery of active proteins into different cell types is an ongoing challenge that when solved would significantly widen the scope of biologics. While methods to deliver proteins in their DNA/RNA forms can provide the proof-of-concept necessary to establish the utility of biologics, they are limited by tightly regulated transcription and translation. Furthermore, protein delivery would allow for better temporal and dose control. Despite the existence of a range of protein-based delivery vehicles, many have been investigated only in a handful of cell types. Delivery into erythrocytes and their precursors warrants increased investigation, as the unique cytoskeleton of these cells leaves them impermeable to a wide variety of cargo. Our work here investigates various delivery vehicles and their inherent ability to mediate protein cargo uptake in erythroid precursors and T-cell lines. We investigated CPMPs, CPPs, CPP additives, bacterial toxins, and contractile injection systems for the delivery into cell lines alongside each other in HUDEP-2 and Jurkat cells.

Generally erythroid lineage showed reduced uptake compared to T-cells, even at high concentrations of cargo; this, highlights the challenge of protein delivery into erythroid precursors. Most delivery vehicles required a minimal concentration of 0.4−1 μM to show significant dose-dependent uptake in either cell type. Once the minimal concentration was reached, the CPMP **ZF5.3** showed the highest uptake in both cell types. While ZF5.3 and E5TAT appeared to be the most potent delivery vehicles, they also showed the largest cell type sensitivity and heterogeneity.

To engineer vehicles more potent for protein delivery to erythroid precursor cells, we investigated the impact of adding IH4, a targeting ligand for GYPA, a highly erythrocyte-specific receptor. We also investigated bacterial delivery vehicles that use receptor targeting for protein delivery (**BoNT** and **PVC**). IH4 appendage improved the potency and selectivity only in conjunction with CPP additives, indicating that receptor targeting across various vehicles may not always be beneficial or that there might be inherent considerations regarding properties of receptors needed (such as endosomal recycling rates and conformational interactions at receptor binding). Widely acknowledged mechanisms of entry and escape of protein DVs highlight the importance of conformation at the membrane surface for entry and could explain the variable response to appending receptor targeting ligand to **ZF5.3**, **E5TAT**, **BoNT**, and **PVC**. Other receptors, ligands, or linker combinations may address these shortcomings, but such optimizations are likely to vary between cell types and cargos. The current work highlights the simplicity and potential generalizability of CPP additives to synergize with receptor-targeting ligands for cell-specific intracellular delivery of protein cargo. A benefit of our method is that **1× TNB-R10** and **3×**

TNB-R10 were added in trans to cargo. This is unlike other vehicles that require genetically or covalently attaching CPPs and CPMPs to the cargo, thereby potentially changing its inherent properties. Furthermore, because **TNB-R10** is appended via disulfide bonds that become reduced in the cytosol to release unmodified cargo.

Recent reports using TNB-R10 indicate that retention of the cargo to the surface is highly correlated to uptake.[57] This likely explains the benefit of adding receptor targeting moieties to the cargo. Our work demonstrates that a 2-fold increase in the surface binding affinity consistently resulted in a 2−3× increase in uptake, as quantified by both confocal microscopy and flow cytometry. While excess CPP additives such as **3× TNB-R10** show improvement in uptake when compared to **1× TNB-R10** with untargeted cargo, this slight improvement is lost when a targeting ligand is appended to the cargo. This suggests that thiol reactivity at the surface of these cell types could be achieved using excess additives or increasing the cargo surface affinity. Additional studies to understand the breadth of receptor-targeting ligand types, affinity for receptors, and delivery conditions would build on these results. Moreover, studies quantifying the amount of active cytosolic concentrations of the delivered cargo are vital to understanding overall efficiency (uptake and endosomal escape). These studies are currently ongoing.

Finally, while the goal of this study was to deliver protein cargo to erythroid progenitors for the selective modulation of disease-associated proteins (e.g., degradation of BCL11A for the induction of fetal hemoglobin), one can also envision loading these cells with cargo that circulating red blood cells can deliver throughout the vasculature.[58] In that instance, it is pertinent to carefully consider the immunological properties of erythroid progenitor cells in suppressing proinflammatory responses of T-cells through modulation of L-arginine[59] or the release of reactive oxygen species and cytokines.[51,60] In summary, this paper evaluates the ability of protein delivery vehicles to mediate cargo uptake to nonmodel cell types such as erythroid progenitors and establishes that receptor targeting does afford selectivity for erythroid lineage cells.

■ ASSOCIATED CONTENT

Supporting Information

The Supporting Information is available free of charge at https://pubs.acs.org/doi/10.1021/acsbiomedchemau.4c00098.

> Figures (page 3) with protein purification gels, mass analysis of TNB-R10, quantification of sulfhydryls, and microscopy images of other treatment conditions. Supporting tables (page 18) of DNA, protein, and primer sequences along with fit curves for Figures 3b-c, 4b, and S4 (PDF)

■ AUTHOR INFORMATION

Corresponding Author

Laura M. K. Dassama − *Department of Chemistry and Sarafan ChEM-H Institute, Stanford University, Stanford, California 94305, United States; Department of Microbiology & Immunology, Stanford School of Medicine, Stanford, California 94305, United States;* orcid.org/0000-0002-0851-6373; Email: dassama@stanford.edu

Authors

Mekedlawit T. Setegne − *Department of Chemistry and Sarafan ChEM-H Institute, Stanford University, Stanford, California 94305, United States*

Aidan T. Cabral − *Department of Bioengineering, Stanford University, Stanford, California 94305, United States*

Anushri Tiwari − *Department of Biology, Stanford University, Stanford, California 94305, United States*

Fangfang Shen − *Department of Chemistry, Stanford University, Stanford, California 94305, United States*

Hawa Racine Thiam − *Sarafan ChEM-H Institute and Department of Bioengineering, Stanford University, Stanford, California 94305, United States; Department of Microbiology & Immunology, Stanford School of Medicine, Stanford, California 94305, United States*

Complete contact information is available at: https://pubs.acs.org/10.1021/acsbiomedchemau.4c00098

Author Contributions

Credit: **Mekedlawit T. Setegne** conceptualization, data curation, formal analysis, investigation, validation, visualization, writing - original draft; **Aidan T. Cabral** data curation, formal analysis, investigation, methodology, visualization, writing - review & editing; **Anushri Tiwari** data curation, investigation; **Fangfang Shen** data curation, formal analysis, investigation, visualization, writing - original draft, writing - review & editing; **Hawa Racine Thiam** conceptualization, data curation, formal analysis, funding acquisition, methodology, resources, supervision, validation, visualization, writing - review & editing; **Laura M. K. Dassama** conceptualization, formal analysis, funding acquisition, project administration, supervision, writing - original draft, writing - review & editing.

Funding

This work is supported in part by NIH grant R01HL173127 (to L.M.K.D.). M.T.S. is supported by Sarafan ChEM-H CBI, DARE, and EDGE fellowships from Stanford University. A.T.C. is supported by Stanford Graduate Fellowship. H.R.T. is supported by the Lazard Fellowship from Stanford University and is a Chan-Zuckerberg Biohub Investigator. L.M.K.D. is supported by a Terman Fellowship from Stanford University, is the David Huntington Dean's Faculty Scholar in the School of Humanities and Sciences, and is the MAC3 Impact Philanthropies Faculty Fellow at the Sarafan ChEM-H Institute.

Notes

The authors declare no competing financial interest.

■ ACKNOWLEDGMENTS

We thank Prof. Alanna Schepartz for providing the plasmid of ZF5.3. We thank Dr. Phillip Kyriakakis for providing the plasmid of mNG. We thank Prof. Alice Ting for providing plasmid of BoNT. We thank Prof. Steven Banik for providing the plasmid of E5TAT. We also thank Ms. Jeandele Elliot, Ms. Lisha Ou, Mr. Jonathan Chou, Mr. Isaac Paddy, Dr. Sandra Ordonez, and Dr. Poulami Chatterjee for helpful discussions. The table of contents (TOC) graphic was created using Biorender.com.

■ REFERENCES

(1) Neklesa, T. K.; Winkler, J. D.; Crews, C. M. Targeted Protein Degradation by PROTACs. *Pharmacol. Ther.* **2017**, *174*, 138−144.

(2) Spradlin, J. N.; Zhang, E.; Nomura, D. K. Reimagining Druggability Using Chemoproteomic Platforms. *Acc. Chem. Res.* **2021**, *54* (7), 1801−1813.

(3) Lu, Y.; Yang, Y.; Zhu, G.; Zeng, H.; Fan, Y.; Guo, F.; Xu, D.; Wang, B.; Chen, D.; Ge, G. Emerging Pharmacotherapeutic Strategies to Overcome Undruggable Proteins in Cancer. *Int. J. Biol. Sci.* **2023**, *19* (11), 3360−3382.

(4) Mullard, A. 2020 FDA Drug Approvals. *Nat. Rev. Drug Discovery* **2021**, *20* (2), 85−90.

(5) Ebrahimi, S. B.; Samanta, D. Engineering Protein-Based Therapeutics through Structural and Chemical Design. *Nat. Commun.* **2023**, *14*, 2411.

(6) Wang, H.; Zhou, R.; Xu, F.; Yang, K.; Zheng, L.; Zhao, P.; Shi, G.; Dai, L.; Xu, C.; Yu, L.; Li, Z.; Wang, J.; Wang, J. Beyond Canonical PROTAC: Biological Targeted Protein Degradation (bioTPD). *Biomater. Res.* **2023**, *27* (1), 72.

(7) Guidotti, G.; Brambilla, L.; Rossi, D. Cell-Penetrating Peptides: From Basic Research to Clinics. *Trends Pharmacol. Sci.* **2017**, *38* (4), 406−424.

(8) Kim, T. K.; Eberwine, J. H. Mammalian Cell Transfection: The Present and the Future. *Anal. Bioanal. Chem.* **2010**, *397* (8), 3173−3178.

(9) Pfeifer, A.; Verma, I. M. Gene Therapy: Promises and Problems. *Annu. Rev. Genomics Hum. Genet.* **2001**, *2* (1), 177−211.

(10) Chan, A.; Tsourkas, A. Intracellular Protein Delivery: Approaches, Challenges, and Clinical Applications. *BME Front* **2024**, *5*, No. 0035.

(11) Jackson, A. L.; Burchard, J.; Schelter, J.; Chau, B. N.; Cleary, M.; Lim, L.; Linsley, P. S. Widespread siRNA "off-Target" Transcript Silencing Mediated by Seed Region Sequence Complementarity. *RNA* **2006**, *12* (7), 1179−1187.

(12) Fu, A.; Tang, R.; Hardie, J.; Farkas, M. E.; Rotello, V. M. Promises and Pitfalls of Intracellular Delivery of Proteins. *Bioconjugate Chem.* **2014**, *25* (9), 1602−1608.

(13) Vaishya, R.; Khurana, V.; Patel, S.; Mitra, A. K. Long-Term Delivery of Protein Therapeutics. *Expert Opin. Drug Delivery* **2015**, *12* (3), 415−440.

(14) Chan, A.; Haley, R. M.; Najar, M. A.; Gonzalez-Martinez, D.; Bugaj, L. J.; Burslem, G. M.; Mitchell, M. J.; Tsourkas, A. Lipid-Mediated Intracellular Delivery of Recombinant bioPROTACs for the Rapid Degradation of Undruggable Proteins. *Nat. Commun.* **2024**, *15* (1), 5808.

(15) Breda, L.; Papp, T. E.; Triebwasser, M. P.; Yadegari, A.; Fedorky, M. T.; Tanaka, N.; Abdulmalik, O.; Pavani, G.; Wang, Y.; Grupp, S. A.; Chou, S. T.; Ni, H.; Mui, B. L.; Tam, Y. K.; Weissman, D.; Rivella, S.; Parhiz, H. In Vivo Hematopoietic Stem Cell Modification by mRNA Delivery. *Science* **2023**, *381* (6656), 436−443.

(16) Banskota, S.; Raguram, A.; Suh, S.; Du, S. W.; Davis, J. R.; Choi, E. H.; Wang, X.; Nielsen, S. C.; Newby, G. A.; Randolph, P. B.; Osborn, M. J.; Musunuru, K.; Palczewski, K.; Liu, D. R. Engineered Virus-like Particles for Efficient *in Vivo* Delivery of Therapeutic Proteins. *Cell* **2022**, *185* (2), 250−265.

(17) Campbell, L. A.; Coke, L. M.; Richie, C. T.; Fortuno, L. V.; Park, A. Y.; Harvey, B. K. Gesicle-Mediated Delivery of CRISPR/Cas9 Ribonucleoprotein Complex for Inactivating the HIV Provirus. *Mol. Ther.* **2019**, *27* (1), 151−163.

(18) Feng, X.; Chang, R.; Zhu, H.; Yang, Y.; Ji, Y.; Liu, D.; Qin, H.; Yin, J.; Rong, H. Engineering Proteins for Cell Entry. *Mol. Pharmaceutics* **2023**, *20* (10), 4868−4882.

(19) Heitz, F.; Morris, M. C.; Divita, G. Twenty Years of Cell-Penetrating Peptides: From Molecular Mechanisms to Therapeutics. *Br. J. Pharmacol.* **2009**, *157* (2), 195−206.

(20) Daniels, D. S.; Schepartz, A. Intrinsically Cell-Permeable Miniature Proteins Based on a Minimal Cationic PPII Motif. *J. Am. Chem. Soc.* **2007**, *129* (47), 14578−14579.

(21) Rabideau, A. E.; Pentelute, B. L. Delivery of Non-Native Cargo into Mammalian Cells Using Anthrax Lethal Toxin. *ACS Chem. Biol.* **2016**, *11* (6), 1490−1501.

(22) Gasparini, G.; Matile, S. Protein Delivery with Cell-Penetrating Poly(Disulfide)s. *Chem. Commun.* **2015**, *51* (96), 17160−17162.

(23) Conner, S. D.; Schmid, S. L. Regulated Portals of Entry into the Cell. *Nature* **2003**, *422* (6927), 37−44.

(24) Teo, S. L. Y.; Rennick, J. J.; Yuen, D.; Al-Wassiti, H.; Johnston, A. P. R.; Pouton, C. W. Unravelling Cytosolic Delivery of Cell Penetrating Peptides with a Quantitative Endosomal Escape Assay. *Nat. Commun.* **2021**, *12* (1), 3721.

(25) Pei, D. How Do Biomolecules Cross the Cell Membrane? *Acc. Chem. Res.* **2022**, *55* (3), 309−318.

(26) Duchardt, F.; Fotin-Mleczek, M.; Schwarz, H.; Fischer, R.; Brock, R. A Comprehensive Model for the Cellular Uptake of Cationic Cell-Penetrating Peptides. *Traffic* **2007**, *8* (7), 848−866.

(27) Appelbaum, J. S.; LaRochelle, J. R.; Smith, B. A.; Balkin, D. M.; Holub, J. M.; Schepartz, A. Arginine Topology Controls Escape of Minimally Cationic Proteins from Early Endosomes to the Cytoplasm. *Chem. Biol.* **2012**, *19* (7), 819−830.

(28) Lee, Y.-J.; Erazo-Oliveras, A.; Pellois, J.-P. Delivery of Macromolecules into Live Cells by Simple Co-Incubation with a Peptide. *Chembiochem Eur. J. Chem. Biol.* **2010**, *11* (3), 325−330.

(29) Qian, L.; Fu, J.; Yuan, P.; Du, S.; Huang, W.; Li, L.; Yao, S. Q. Intracellular Delivery of Native Proteins Facilitated by Cell-Penetrating Poly(Disulfide)s. *Angew. Chem., Int. Ed.* **2018**, *57* (6), 1532−1536.

(30) Roh, H.; Dorner, B. G.; Ting, A. Y. Cell-Type-Specific Intracellular Protein Delivery with Inactivated Botulinum Neurotoxin. *J. Am. Chem. Soc.* **2023**, *145* (18), 10220−10226.

(31) Kreitz, J.; Friedrich, M. J.; Guru, A.; Lash, B.; Saito, M.; Macrae, R. K.; Zhang, F. Programmable Protein Delivery with a Bacterial Contractile Injection System. *Nature* **2023**, *616* (7956), 357−364.

(32) Mueller, J.; Kretzschmar, I.; Volkmer, R.; Boisguerin, P. Comparison of Cellular Uptake Using 22 CPPs in 4 Different Cell Lines. *Bioconjugate Chem.* **2008**, *19* (12), 2363−2374.

(33) Harayama, T.; Riezman, H. Understanding the Diversity of Membrane Lipid Composition. *Nat. Rev. Mol. Cell Biol.* **2018**, *19* (5), 281−296.

(34) Cooper, G. M. Cell Membranes. In *The Cell: A Molecular Approach*, 2nd ed.; Sinauer Associates, 2000.

(35) Alberts, B.; Johnson, A.; Lewis, J.; Raff, M.; Roberts, K.; Walter, P. Membrane Proteins. In *Molecular Biology of the Cell*, 4th ed.; Garland Science, 2002.

(36) Renne, M. F.; Ernst, R. Membrane Homeostasis beyond Fluidity: Control of Membrane Compressibility. *Trends Biochem. Sci.* **2023**, *48* (11), 963−977.

(37) Himbert, S.; D'Alessandro, A.; Qadri, S. M.; Majcher, M. J.; Hoare, T.; Sheffield, W. P.; Nagao, M.; Nagle, J. F.; Rheinstädter, M. C. The Bending Rigidity of the Red Blood Cell Cytoplasmic Membrane. *PLoS One* **2022**, *17* (8), No. e0269619.

(38) Li, H.; Lykotrafitis, G. Erythrocyte Membrane Model with Explicit Description of the Lipid Bilayer and the Spectrin Network. *Biophys. J.* **2014**, *107* (3), 642−653.

(39) Orkin, S. H.; Bauer, D. E. Emerging Genetic Therapy for Sickle Cell Disease. *Annu. Rev. Med.* **2019**, *70*, 257−271.

(40) Shen, F.; Zheng, G.; Setegne, M.; Tenglin, K.; Izadi, M.; Xie, H.; Zhai, L.; Orkin, S. H.; Dassama, L. M. K. A Cell-Permeant Nanobody-Based Degrader That Induces Fetal Hemoglobin. *ACS Cent. Sci.* **2022**, *8* (12), 1695−1703.

(41) Giger, K.; Habib, I.; Ritchie, K.; Low, P. S. Diffusion of Glycophorin A in Human Erythrocytes. *Biochim. Biophys. Acta* **2016**, *1858* (11), 2839−2845.

(42) Uhlén, M.; Fagerberg, L.; Hallström, B. M.; Lindskog, C.; Oksvold, P.; Mardinoglu, A.; Sivertsson, Å.; Kampf, C.; Sjöstedt, E.; Asplund, A.; Olsson, I.; Edlund, K.; Lundberg, E.; Navani, S.; Szigyarto, C. A.-K.; Odeberg, J.; Djureinovic, D.; Takanen, J. O.; Hober, S.; Alm, T.; Edqvist, P.-H.; Berling, H.; Tegel, H.; Mulder, J.; Rockberg, J.; Nilsson, P.; Schwenk, J. M.; Hamsten, M.; von Feilitzen, K.; Forsberg, M.; Persson, L.; Johansson, F.; Zwahlen, M.; von Heijne, G.; Nielsen, J.; Pontén, F. Tissue-Based Map of the Human Proteome. *Science* **2015**, *347* (6220), No. 1260419.

(43) Chasis, J.; Mohandas, N. Red Blood Cell Glycophorins. *Blood* **1992**, *80* (8), 1869−1879.

(44) Habib, I.; Smolarek, D.; Hattab, C.; Grodecka, M.; Hassanzadeh-Ghassabeh, G.; Muyldermans, S.; Sagan, S.; Gutiérrez, C.; Laperche, S.; Le-Van-Kim, C.; Aronovicz, Y. C.; Wasniowska, K.; Gangnard, S.; Bertrand, O. V(H)H (Nanobody) Directed against Human Glycophorin A: A Tool for Autologous Red Cell Agglutination Assays. *Anal. Biochem.* **2013**, *438* (1), 82−89.

(45) Schneider, A. F. L.; Kithil, M.; Cardoso, M. C.; Lehmann, M.; Hackenberger, C. P. R. Cellular Uptake of Large Biomolecules Enabled by Cell-Surface-Reactive Cell-Penetrating Peptide Additives. *Nat. Chem.* **2021**, *13* (6), 530−539.

(46) Raghupathi, K.; Thayumanavan, S. Chapter Sixteen - Nano-Armoring of Enzymes: Rational Design of Polymer-Wrapped Enzymes. In *Methods in Enzymology*; Kumar, C. V., Ed.; NanoArmoring of Enzymes: Rational Design of Polymer-Wrapped Enzymes; Academic Press, 2017; Vol. *590*, pp 381−411. DOI: 10.1016/bs.mie.2017.01.007.

(47) LaRochelle, J. R.; Cobb, G. B.; Steinauer, A.; Rhoades, E.; Schepartz, A. Fluorescence Correlation Spectroscopy Reveals Highly Efficient Cytosolic Delivery of Certain Penta-Arg Proteins and Stapled Peptides. *J. Am. Chem. Soc.* **2015**, *137* (7), 2536−2541.

(48) Yoshida, S. R.; Maity, B. K.; Chong, S. Visualizing Protein Localizations in Fixed Cells: Caveats and the Underlying Mechanisms. *J. Phys. Chem. B* **2023**, *127* (19), 4165−4173.

(49) Dzierzak, E.; Philipsen, S. Erythropoiesis: Development and Differentiation. *Cold Spring Harb. Perspect. Med.* **2013**, *3* (4), a011601.

(50) Zivot, A.; Lipton, J. M.; Narla, A.; Blanc, L. Erythropoiesis: Insights into Pathophysiology and Treatments in 2017. *Mol. Med.* **2018**, *24* (1), 11.

(51) Grzywa, T. M.; Nowis, D.; Golab, J. The Role of CD71+ Erythroid Cells in the Regulation of the Immune Response. *Pharmacol. Ther.* **2021**, *228*, No. 107927.

(52) Broudy, V. C.; Lin, N.; Brice, M.; Nakamoto, B.; Papayannopoulou, T. Erythropoietin Receptor Characteristics on Primary Human Erythroid Cells. *Blood* **1991**, *77* (12), 2583−2590.

(53) Chasis, J. A.; Mohandas, N. Red Blood Cell Glycophorins. *Blood* **1992**, *80* (8), 1869−1879, DOI: 10.1182/blood.V80.8.1869.1869.

(54) Lee, J.; Vernet, A.; Redfield, K.; Lu, S.; Ghiran, I. C.; Way, J. C.; Silver, P. A. Rational Design of a Bifunctional AND-Gate Ligand To Modulate Cell−Cell Interactions. *ACS Synth. Biol.* **2020**, *9* (2), 191−197.

(55) Pirazzini, M.; Rossetto, O.; Eleopra, R.; Montecucco, C. Botulinum Neurotoxins: Biology, Pharmacology, and Toxicology. *Pharmacol. Rev.* **2017**, *69* (2), 200−235.

(56) Geller, A. M.; Pollin, I.; Zlotkin, D.; Danov, A.; Nachmias, N.; Andreopoulos, W. B.; Shemesh, K.; Levy, A. The Extracellular Contractile Injection System Is Enriched in Environmental Microbes and Associates with Numerous Toxins. *Nat. Commun.* **2021**, *12* (1), 3743.

(57) Arafiles, J. V. V.; Franke, J.; Franz, L.; Gomez-Gonzalez, J.; Kemnitz-Hassanin, K.; Hackenberger, C. P. R. Cell-Surface-Retained Peptide Additives for the Cytosolic Delivery of Functional Proteins. *J. Am. Chem. Soc.* **2023**, *145* (45), 24535−24548.

(58) Villa, C. H.; Anselmo, A. C.; Mitragotri, S.; Muzykantov, V. Red Blood Cells: Supercarriers for Drugs, Biologicals, and Nanoparticles and Inspiration for Advanced Delivery Systems. *Adv. Drug Delivery Rev.* **2016**, *106* (PtA), 88−103.

(59) Elahi, S.; Ertelt, J. M.; Kinder, J. M.; Jiang, T. T.; Zhang, X.; Xin, L.; Chaturvedi, V.; Strong, B. S.; Qualls, J. E.; Steinbrecher, K. A.; Kalfa, T. A.; Shaaban, A. F.; Way, S. S. Immunosuppressive CD71+ Erythroid Cells Compromise Neonatal Host Defence against Infection. *Nature* **2013**, *504* (7478), 158−162.

(60) Elahi, S. Neglected Cells: Immunomodulatory Roles of CD71+ Erythroid Cells. *Trends Immunol.* **2019**, *40* (3), 181−185.